



Cite this: *Energy Environ. Sci.*, 2025, **18**, 2025

## Catalyst–electrolyte interface engineering propels progress in acidic CO<sub>2</sub> electroreduction

Yunling Jiang, Linsen Huang, Chaojie Chen, Yao Zheng \* and Shi-Zhang Qiao \*

The electrocatalytic carbon dioxide reduction reaction (CO<sub>2</sub>RR) is a viable strategy that supports carbon neutrality *via* transforming the dominant greenhouse gas CO<sub>2</sub> into high-value-added chemicals. The CO<sub>2</sub>RR in alkaline and neutral media has thrived in recent years owing to their high CO<sub>2</sub> solubility and favourable CO<sub>2</sub> activation ability. However, critical challenges have emerged, such as carbonate formation and subsequent CO<sub>2</sub> crossover to the anodic sides, which decreases the carbon efficiency and stability of the system. Alternatively, acidic media provide an advantageous environment to prevent CO<sub>2</sub> crossover into the anolyte but suffers from strong HER competition, which is significantly more active under acidic conditions, largely reducing the CO<sub>2</sub> conversion efficiency. Research on acidic CO<sub>2</sub>RRs began with some basic studies, including testing various catalysts and electrolytes and designing diverse substrate structures. With advancements in characterization technologies, it has been found that the acidic CO<sub>2</sub>RR is not only influenced by variations in the composition of the catalyst, substrate or electrolyte, but also by internal changes at the catalyst–electrolyte interface. Thus, catalyst–electrolyte interface engineering, involving electrolyte engineering, catalyst modification, and interface optimization, provides many feasible solutions for acidic CO<sub>2</sub>RRs to weaken the competing HER. Importantly, it extends acidic CO<sub>2</sub>RR investigation to the exploration of electronic structures, interfacial adsorption of cations and anions, and surface hydrophobicity of catalysts in the presence of an electric field. However, there are limited articles reviewing acidic CO<sub>2</sub>RRs from this perspective, and thus, this review aims to discuss the challenges, history, evaluation, and breakthroughs in acidic CO<sub>2</sub>RRs regarding catalyst–electrolyte interface engineering, thereby providing insights for the future development of acidic CO<sub>2</sub>RRs.

Received 4th December 2024,  
Accepted 27th January 2025

DOI: 10.1039/d4ee05715e

rsc.li/ees

### Broader context

Relentless utilization of fossil fuels has caused the accumulation of greenhouse gases, driving global warming and subsequent natural disasters. Carbon dioxide (CO<sub>2</sub>), as a major greenhouse gas, demands innovative strategies for efficient conversion to achieve carbon neutrality. Powered by renewable electricity, the electrocatalytic CO<sub>2</sub> reduction reaction (CO<sub>2</sub>RR) provides promising technology to transform CO<sub>2</sub> into high-value-added chemicals, thereby promoting a sustainable carbon cycle. In the advancement of CO<sub>2</sub>RRs, alkaline and neutral media took precedence owing to their high CO<sub>2</sub> solubility, effective CO<sub>2</sub> activation ability and excellent efficiency. However, alkaline and neutral CO<sub>2</sub>RR processes suffer from issues such as carbonate formation and carbon crossover, compromising system stability and conversion efficiency. Thus, the acidic CO<sub>2</sub>RR has emerged as a promising alternative, although it still faces challenges such as competing hydrogen evolution and limited CO<sub>2</sub>RR intermediate adsorption. Developments in catalyst–electrolyte interface engineering are crucial to overcoming the obstacles in acidic CO<sub>2</sub>RRs. Focusing on catalyst–electrolyte interface engineering, this review highlights the development challenges and trajectory of the acidic CO<sub>2</sub>RR, outlines its evaluation metrics, and summarizes the ongoing efforts in the development of the acidic CO<sub>2</sub>RR. Furthermore, a concluding overview of the current limitations in the acidic CO<sub>2</sub>RR and an outlook on the future development of this research field are proposed.

## 1. Introduction

With the rapid development of global industrialization, the emission of global greenhouse gases has reached a historic

high level.<sup>1</sup> As a key greenhouse gas, carbon dioxide (CO<sub>2</sub>) emission has surged to as high as 540 billion tons annually, resulting in an unprecedented acceleration in global warming.<sup>2</sup> On the path to achieving carbon neutrality and zero emissions, the electrochemical carbon dioxide reduction reaction (CO<sub>2</sub>RR) powered by renewable electricity offers a feasible technology for converting CO<sub>2</sub> into high-value-added chemicals, thereby

School of Chemical Engineering, The University of Adelaide, Adelaide, SA 5005, Australia. E-mail: [yao.zheng01@adelaide.edu.au](mailto:yao.zheng01@adelaide.edu.au), [s.qiao@adelaide.edu.au](mailto:s.qiao@adelaide.edu.au)

advancing carbon capture and utilization.<sup>3–5</sup> Taking advantage of the high solubility of CO<sub>2</sub> and superior ability for CO<sub>2</sub> activation, alkaline and neutral CO<sub>2</sub>RRs, which can significantly suppress hydrogen evolution reaction (HER), dominate the development of CO<sub>2</sub>RRs.<sup>6,7</sup> As device technology advances, including the development of flow cells coupled with gas diffusion electrodes (GDE) and membrane electrode assemblies (MEAs), CO<sub>2</sub>RR systems with excellent performance in alkaline and neutral environments proliferate.<sup>8–10</sup> Notably, long-term



**Yunling Jiang**

*Yunling Jiang received her BS degree and MS degree from Central South University. She is now a PhD candidate in the School of Chemical Engineering, The University of Adelaide. Her research focuses on the exploration of strategies for high-performance electrochemical CO<sub>2</sub> reduction.*



**Linsen Huang**

*Linsen Huang is a PhD candidate in the School of Chemical Engineering at The University of Adelaide. His research is centred around the design and optimization of electrocatalysts, with a particular focus on understanding the underlying mechanisms involved in alkyne electrocatalysis.*

stability of 2400 h (10 days) has been achieved by homogeneously alloyed Bi<sub>0.1</sub>Sn crystals for CO<sub>2</sub>-to-formate conversion under alkaline conditions.<sup>11</sup> Meanwhile, as a significant breakthrough, pure-water-fed CO<sub>2</sub>RRs demonstrated over 1000 h of operation on a surface-step-rich Cu catalyst with a 50% faradaic efficiency (FE) for ethylene at a total current of 10 A using a scaled-up electrolyser stack.<sup>12</sup> Advancements in the selectivity for single products have continuously emerged in alkaline and neutral media, including CO, formic acid, CH<sub>4</sub>, ethanol and ethylene, with FE exceeding 90% for single-carbon products, such as CO and formate, and FE of over 70% for double-carbon products, such as ethanol and ethylene.<sup>13–17</sup> Particularly, several studies achieved promising progress in CO<sub>2</sub>RR toward triple-carbon products. The production of propane with a high FE of 91% was achieved on a 1-ethyl-3-methylimidazolium-functionalized Mo<sub>3</sub>P nanocatalyst.<sup>18</sup> A co-electrodeposited CuAg alloy catalyst could produce 2-propanol with an FE of 56.7% at 59.3 mA cm<sup>-2</sup>.<sup>19</sup> Nevertheless, a fatal weakness of alkaline and neutral CO<sub>2</sub>RR has exposed, *i.e.*, the inevitable generation of carbonate due to the reaction between OH<sup>–</sup> and CO<sub>2</sub>, which can cross over into the anolyte, resulting in CO<sub>2</sub> loss and reduced carbon conversion efficiency.<sup>20,21</sup> Also, the generated carbonate increases the resistance of the operation system and blocks the gas diffusion channels, leading to



**Chaojie Chen**

*Chaojie Chen is currently a PhD student in the School of Chemical Engineering, The University of Adelaide. His research focuses on the design of electrocatalysts and mechanisms of electrocatalysis.*



**Yao Zheng**

*Yao Zheng received his PhD in 2014 from the University of Queensland (Australia). He is currently a Professor at The University of Adelaide. His current research focuses on fundamental studies of some key electrocatalysis processes by combining experiments and theoretical computations and the development of advanced electrocatalysts for energy conversion processes.*



**Shi-Zhang Qiao**

*Shi-Zhang Qiao received his PhD in Chemical Engineering from the Hong Kong University of Science and Technology in 2000. He is currently a Chair Professor, elected Fellow of the Australian Academy of Science, ARC Industry Laureate Fellow, and ARC Australian Laureate Fellow at the School of Chemical Engineering, The University of Adelaide (Australia). His research expertise is in nanomaterials for new energy technologies (electrocatalysis, photocatalysis and batteries).*

additional reaction energy consumption and unnecessary cost of electrolyte reuse.<sup>21,22</sup> Consequently, the industrialization of alkaline/neutral CO<sub>2</sub>RR encounters significant obstacles.

In contrast to alkaline and neutral CO<sub>2</sub>RR, CO<sub>2</sub>RR in an acidic environment can prevent carbonate generation and CO<sub>2</sub> crossover issues, enhancing the carbon efficiency and electrode stability. Thus, electrocatalytic CO<sub>2</sub>RR in acid media has gained increasing popularity recently.<sup>23–25</sup> In fact, the initial attempt to perform acidic CO<sub>2</sub>RR was reported in 2001. Yano *et al.* pioneered an electrocatalytic reaction system featuring a gas-liquid-solid three-phase interface.<sup>26</sup> Also, they examined the influence of different pH values and K<sup>+</sup> ion concentrations in the electrolyte, as well as the halide composition in the electrodes on the CO<sub>2</sub>RR product selectivity.<sup>26–28</sup> Thereafter, the development of acidic CO<sub>2</sub>RR was dormant for approximately ten years. However, with the identification of numerous practical challenges regarding alkaline and neutral CO<sub>2</sub>RR, acidic CO<sub>2</sub>RR has regained attention. Nevertheless, acidic CO<sub>2</sub>RR has encountered substantial hurdles, including intense competition with the HER and limited adsorption of the CO<sub>2</sub>RR intermediates, resulting in unsatisfactory product selectivity.<sup>29</sup> Specifically, in acidic media, high-concentration H<sup>+</sup> ions in the electrolyte compete with CO<sub>2</sub>RR-promoted intermediates to adsorb on the catalyst surface, aggravating the hydrogen evolution reaction (HER). Generally, the aggravated HER competition leads to a reduction in the FE for the CO<sub>2</sub>RR products, while increasing the selectivity for H<sub>2</sub>. Additionally, owing to the unstable adsorption of the CO<sub>2</sub>RR-promoted intermediates (\*CO, \*CHO, etc.) in acidic media, it becomes more difficult for the acidic CO<sub>2</sub>RR to support long-chain reaction pathways and produce multi-carbon (C<sub>2+</sub>) products compared to alkaline and neutral conditions. Therefore, it is crucial to develop strategies that can significantly enhance the acidic CO<sub>2</sub>RR, while effectively suppressing hydrogen evolution.

Unlike the initial development stage focusing on the basic exploration of simple component replacement in electrocatalysts and electrolytes for acidic CO<sub>2</sub>RR, advancements in various interface characterization techniques have further broadened the understanding of acidic CO<sub>2</sub>RR by highlighting the significant impacts of catalyst-electrolyte interfaces.<sup>30–32</sup> Specifically, it is acknowledged that the alkali metal cations in alkaline and neutral CO<sub>2</sub>RR are closely related to the intermediate stabilization and reaction efficiency.<sup>33,34</sup> However, unlike in alkaline and neutral electrolytes, in which alkali metal ions are inherently present, acidic electrolytes contain no alkali metal ions. Therefore, motivated by the role of alkali metal cations in alkaline and neutral CO<sub>2</sub>RR, the effects of varying concentrations and types of alkali metal cations on the catalyst-electrolyte interface were investigated in acidic CO<sub>2</sub>RR by introducing alkali metal salts into acidic electrolytes.<sup>35–37</sup> Studies on catalyst-electrolyte engineering demonstrate that introducing high concentrations of alkali metal salts into acid electrolytes can induce cation aggregation on the catalyst surface under an electric field.<sup>25,37,38</sup> The interfacial cations,

especially K<sup>+</sup> and Cs<sup>+</sup>, can effectively enhance the adsorption of \*OH and impede proton transfer. Thus, a localized alkaline environment, namely a spatially confined and transient high-pH area on the catalyst surface, can be constructed, suppressing the competing HER.<sup>24,36,39</sup> It should be noted that in contrast to the bulk pH governed by the electrolyte composition and concentration, the local alkalinity is subject to the reaction kinetics and local ion flux.<sup>40</sup> Subsequent research integrated the cation effect with catalyst modification in electronic structures or interface hydrophobicity engineering to synergistically enhance the stability of the alkaline local environment and the adsorption of the relevant intermediates on the catalyst-electrolyte interface for acidic CO<sub>2</sub>RR.<sup>23,41–44</sup> However, it is worth noting that due to a high local alkalinity, such high concentration of alkali metal cations in the electrolyte, can lead to the generation of carbonate and crystallization on the electrode, hindering gas transport and threatening the long-term stability of the whole reaction system.<sup>38,45,46</sup> Thus, to thoroughly prevent salt crystallization caused by carbonate generation, some researchers have focused on developing acidic CO<sub>2</sub>RR systems using alkali metal ion-free electrolytes (pure acid) by directly immobilizing cation groups on the surface of the catalyst.<sup>45,47,48</sup> Nevertheless, the stability of long-chain cation groups and the high energy barrier for CO<sub>2</sub>RR in pure acid electrolytes restrict the operation current density to below 300 mA cm<sup>-2</sup>. In short, catalyst-electrolyte interface engineering has advanced the development of acidic CO<sub>2</sub>RR; however, challenges are still emerging continuously.

Given that comprehensive reviews summarizing and categorizing these developments are limited, instead of focusing on the type of catalyst or electrolyte, this review systematically examines the developmental trajectory of acidic CO<sub>2</sub>RR by discussing the complex interactions between the catalyst and electrolyte, namely, the engineering of the catalyst-electrolyte interface. By discussing the reaction system and mechanism challenges for acidic CO<sub>2</sub>RR, the importance of modulating the catalyst-electrolyte interface is underscored. Moreover, the developmental history of acidic CO<sub>2</sub>RR highlights the significance of the investigation of the catalyst-electrolyte interfaces. Besides, beyond the common parameters for CO<sub>2</sub>RR, some evaluation metrics associated with interfacial properties specific to acidic CO<sub>2</sub>RR are also summarized. Extensively, the propelling effects on acidic CO<sub>2</sub>RR *via* catalyst-electrolyte interface engineering are comprehensively reviewed based on three key aspects including electrolyte engineering, catalyst modification and interface optimization. Finally, we present a conclusive overview of existing contradictions and constraints in acidic CO<sub>2</sub>RR, together with an outlook on the future research directions and perspectives in this field.

## 2. Challenges in acidic CO<sub>2</sub>RR

Despite the significant advancements and continuous emerging results in CO<sub>2</sub> electroreduction under alkaline and neutral

conditions, inevitable issues such as the formation of carbonate and subsequent carbon crossover continue to pose significant challenges. Thus, these drawbacks have driven the revitalization of acidic CO<sub>2</sub>RR. However, chronic problems and challenges of acidic CO<sub>2</sub>RR, such as competing HER, weak adsorption of CO<sub>2</sub>RR intermediates, and sluggish CO<sub>2</sub>RR kinetics, still exist and require the application of cutting-edge technologies for analysis. In this chapter, we comprehensively discuss these challenges with regards to the reaction systems and mechanisms.

## 2.1 Reaction systems

From a kinetic perspective, it is preferable for the CO<sub>2</sub>RR process to take place in alkaline and near-neutral environments, owing to the effective activation of CO<sub>2</sub>, reduced HER competition and enhanced CO<sub>2</sub>RR product selectivity.<sup>21,35,49,50</sup> However, although the primary species in the alkaline system at the start of electrolysis are just the KOH electrolyte and CO<sub>2</sub> reactant, it is inevitable for these two species to react and form carbonate (KHCO<sub>3</sub> or K<sub>2</sub>CO<sub>3</sub>) during prolonged electrolysis (OH<sup>-</sup> + CO<sub>2</sub> → HCO<sub>3</sub><sup>-</sup> and 2OH<sup>-</sup> + CO<sub>2</sub> → CO<sub>3</sub><sup>2-</sup> + H<sub>2</sub>O, Fig. 1a).<sup>21,51</sup> The generation of carbonate will lead to carbon crossover to the anode side and salt participation on the electrode, significantly reducing the carbon efficiency and blocking the gas transport channels.<sup>52</sup> Also, when KHCO<sub>3</sub> is utilized as the neutral electrolyte for CO<sub>2</sub>RR, OH<sup>-</sup> can be generated during CO<sub>2</sub> reduction (CO<sub>2</sub> + H<sub>2</sub>O + 2e<sup>-</sup> → CO + 2OH<sup>-</sup>) and H<sub>2</sub>O decomposition (H<sub>2</sub>O + 2e<sup>-</sup> → H<sub>2</sub> + OH<sup>-</sup>).<sup>53</sup> Therefore, carbonate formation and carbon crossover are also unavoidable (Fig. 1b). Additionally, the increase in cell voltage

under neutral conditions, resulting from the high overpotential of the oxygen evolution reaction (OER), leads to additional energy consumption.<sup>54</sup> Thus, based on the discussion above, carbonate generation is a common issue in both alkaline and neutral CO<sub>2</sub>RR, resulting in carbon crossover during continuous electrolysis. These issues can result in a significantly lower CO<sub>2</sub> single-pass conversion efficiency (SPCE), threaten the device operation stability, and even cause higher energy consumption for large-scale applications. Consequently, addressing the carbonate formation issue is essential to achieve an economically viable CO<sub>2</sub> electroreduction. When operating CO<sub>2</sub>RR in the acidic mode (Fig. 1c), OH<sup>-</sup> anions can still be generated during the reaction operation and react with CO<sub>2</sub>, leading to the formation of unwanted carbonate salts near the cathode. Ingeniously, the acidic environment will consume these carbonate salts and convert them back into CO<sub>2</sub>, preventing the carbon loss issue.<sup>55,56</sup> Thus, in theory, the CO<sub>2</sub> SPCE of strongly acidic CO<sub>2</sub>RR is 100%. Due to the high conductivity of strong acid and the efficient acidic OER kinetics, the increased cell voltage issue under neutral conditions can also be alleviated, benefiting the energy efficiency (EE).<sup>6</sup> However, there are always two sides to consider. It is obvious that acidic CO<sub>2</sub>RR is challenging due to the intense HER competition, resulting from the kinetically favourable H<sup>+</sup> transport in strong acids.<sup>57</sup> Thus, HER tends to dominate on most catalysts in pure acid, significantly obstructing CO<sub>2</sub>RR.

## 2.2 Reaction mechanisms

As mentioned above, alkaline and neutral environments are more advantageous for CO<sub>2</sub> activation, resulting in high

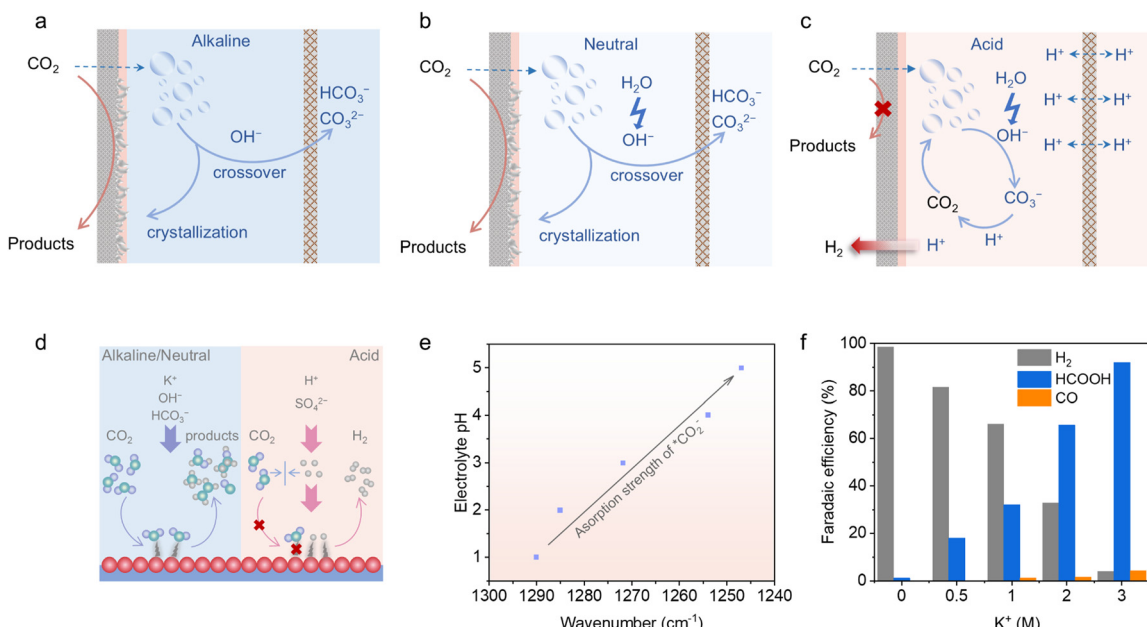


**Fig. 1** Schematic of the internal carbonate generation and crossover phenomena in (a) alkaline and (b) neutral CO<sub>2</sub>RRs. (c) Schematic of the internal carbonate-free operation in an acidic CO<sub>2</sub>RR. (d) Differences in intermediate adsorption in alkaline, neutral and acidic media. (e) Variations in CO<sub>2</sub> binding strength with changes in electrolyte pH.<sup>58</sup> (f) FEIs of CO<sub>2</sub>RR products on a Bi nanosheet catalyst in a 0.05 M H<sub>2</sub>SO<sub>4</sub> catholyte with different KCl concentrations, showing the effect of K<sup>+</sup> on suppressing the HER.<sup>59</sup> Reproduced with permission from ref. 59. Copyright 2022, the American Chemical Society.

selectivity for the CO<sub>2</sub>RR products. In contrast, in acidic CO<sub>2</sub>RR, the bulk system will fill with H<sup>+</sup> ions, which can be adsorbed on the cathode as \*H during the reduction process, further leading to the dominance of H<sub>2</sub> among the released products (Fig. 1d).<sup>45</sup> Then, it is of high difficulty for the CO<sub>2</sub> molecules to contact with the active sites and become adsorbed \*CO<sub>2</sub> species in pure acid. Besides, CO<sub>2</sub>RR-related intermediates tend to bind weakly and unstably in acidic media, making them prone to easy desorption, which further diminishes the reaction efficiency. As shown in Fig. 1e, the reaction intermediates of acidic CO<sub>2</sub>RR on Sn single-atom catalysts were manifested and compared under different pH values and reduction potentials through *in situ* attenuated total reflection Fourier transform infrared (ATR-FTIR) spectroscopy.<sup>58</sup> It can be observed that the surface coverage of \*CO<sub>2</sub> was promoted with an increase in the pH value, and simultaneously the \*CO<sub>2</sub> adsorption strength on the catalyst was enhanced following the improvement in alkalinity. Therefore, the priority for advancing acidic CO<sub>2</sub>RR is to establish an interfacial alkaline microenvironment that strengthens \*CO<sub>2</sub> adsorption, while weakening \*H adsorption even within acidic bulk electrolyte systems.

In terms of the reaction system and mechanism challenges for acidic CO<sub>2</sub>RR, introducing high-concentration alkali metal cations in acidic electrolytes stands as an effective solution to suppress the competing HER and reduce \*H adsorption. Research revealed that alkali cations from the electrolyte can adsorb onto the catalyst-electrolyte surface under the influence of an electric field during acidic CO<sub>2</sub>RR processes.<sup>37,49</sup> This cation effect can facilitate the adsorption and accumulation of \*OH, while suppressing the H<sup>+</sup> diffusion, which subsequently elevates the local alkalinity. As a result, the HER competition can be suppressed, and the adsorption of CO<sub>2</sub>RR-related intermediates can be promoted, favouring the CO<sub>2</sub>RR process in acidic media (Fig. 1f).<sup>23,45,60,61</sup> Further, an increasing number of studies combined catalyst structural optimization with the introduction of high-concentration alkali metal salts into acidic electrolytes to effectively regulate the catalyst-electrolyte interface and achieve high-performance acidic CO<sub>2</sub>RR.<sup>23,42,62</sup> However, careful concentration modulation of the added alkali-metal cations is necessary. It was reported that an alkali-metal cation concentration of at least 2 M is typically sufficient to enhance CO<sub>2</sub>RR product formation, especially for the production of multi-carbon products.<sup>25</sup> Nevertheless, the increase in local alkalinity driven by the addition of high-concentration alkali metal salts can result in generation and crystallization of carbonate on the catalyst-electrolyte interface. Therefore, even if the carbon crossover is well addressed in the acidic mode, the gas diffusion channel blocking issue still exists.<sup>38,45</sup> Given this situation, it is required to explore strategies to decrease the concentration of alkali metal salts, while maintaining a comparable acidic CO<sub>2</sub>RR performance. Some studies introduced additional cation-enriched layers on the catalyst-electrolyte surface to increase the interfacial cation concentration in the bulk electrolyte with a low cation concentration, constructing a balanced trade-off between the cation concentration and acidic

CO<sub>2</sub>RR performance.<sup>63</sup> Furthermore, several researchers focused on alkali metal cation-free acidic CO<sub>2</sub>RR by immobilizing long-chain cation groups on the cathode surface.<sup>45,47,48</sup> However, maintaining the stability of the cation-augment layers over long-term and high-current reaction processes is difficult. Additionally, it is extremely challenging to achieve high CO<sub>2</sub>RR product selectivity in pure acid. As a result, reports in this field are limited and this research direction remains in its early stages.

In short, although the research field of acidic CO<sub>2</sub>RR is developing rapidly as the understanding of the catalyst-electrolyte interface expands, challenges continue to emerge. Currently, a foolproof solution for achieving high-performance and long-term acidic CO<sub>2</sub>RR is still lacking.

### 3. Development history of acidic CO<sub>2</sub>RR

As feasible technology to achieve carbon neutrality, CO<sub>2</sub>RR has undergone decades of development with continuous innovations in terms of catalysts, electrolytes, and electrolyzers. These advancements have enabled breakthroughs in the challenging acidic CO<sub>2</sub>RR. The acidic CO<sub>2</sub>RR has been in development for more than twenty years, undergoing different stages including preliminary attempts, subsequent stagnation, and recent resurgence (Fig. 2a). This chapter will retrospect the development history of acidic CO<sub>2</sub>RR chronologically, alongside the evolution of the electrolyzers and key perspectives.

#### 3.1 Preliminary attempts (2002–2004)

During the early research stage of acidic CO<sub>2</sub>RR, the main challenge was the limited CO<sub>2</sub> concentration near the electrode due to the low solubility of CO<sub>2</sub> in acid solution and the two-phase (liquid–solid) interface electrolysis system. In the early 21st century, to increase the CO<sub>2</sub> concentration at the cathode interface, Yano *et al.* developed an electrolysis cell featuring a three-phase interface (gas–liquid–solid), in which CO<sub>2</sub> gas can be pressed and contacted with the working cathode through a glass filter.<sup>65</sup> This led to substantial advances in the acidic CO<sub>2</sub>RR. Capitalizing on the momentum, Yano and colleagues conducted further in-depth explorations, including the promoting effect of three-phase interfaces on both Cu and Ag-based catalysts, as well as the time and pH dependence of acidic CO<sub>2</sub>RR.<sup>26,65</sup> Additionally, they studied CO<sub>2</sub> conversion in electrolytes containing different types and concentrations of cations and anions.<sup>26</sup> Furthermore, they delved into the effects of introducing Cu<sup>2+</sup> ions in the electrolyte and doping different halogens into Cu on the acidic CO<sub>2</sub>RR.<sup>27,28</sup> As pioneers in the field of acidic CO<sub>2</sub>RR, they proved that three-phase interface reaction system is more effective than the two-phase system in acidic CO<sub>2</sub>RR. In addition, they found that potassium cations (K<sup>+</sup>) and higher concentrations of cations are conducive to producing more multi-carbon products. Also, they demonstrated that feeding Cu<sup>2+</sup> into electrolyte and doping halogens, especially Br, can promote ethylene production on Cu catalysts.

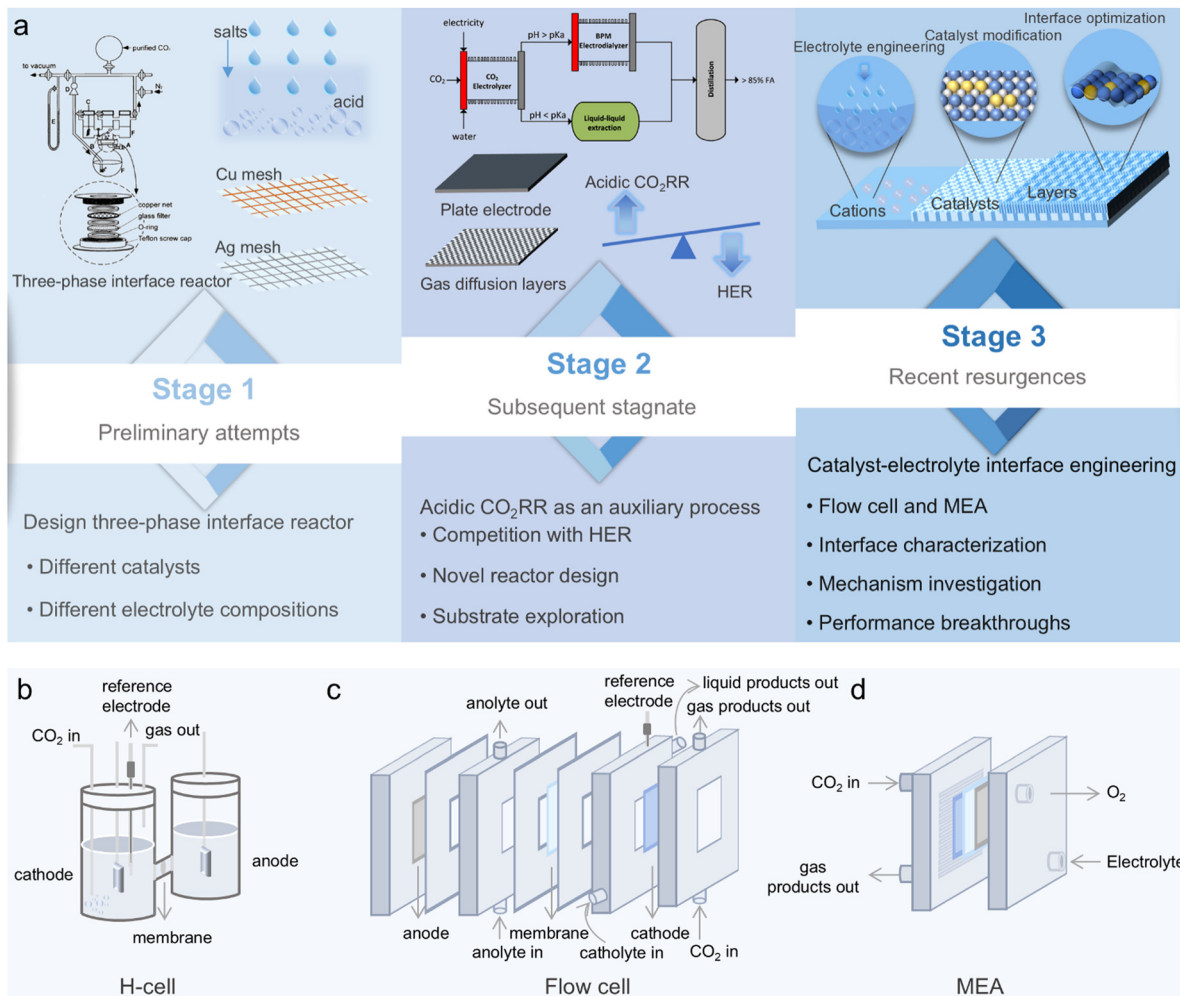


Fig. 2 (a) Development progress of the acidic CO<sub>2</sub>RR.<sup>26,64</sup> Reproduced with permission from ref. 26. Copyright 2002, Elsevier. Schematic configuration of CO<sub>2</sub>RR electrolyser development: (b) H-cell, (c) flow cell, and (d) MEA.

Although their research merely focused on the direct relationship between the acidic CO<sub>2</sub>RR production and the catalyst/electrolyte composition, the findings laid the foundation for the subsequent advancement in the acidic CO<sub>2</sub>RR field.

### 3.2 Subsequent stagnation (2005–2020)

After the initial attempt to perform acidic CO<sub>2</sub>RR, this research area remained dormant for nearly a decade. Following this decade-long hiatus, some intermittent studies on acidic CO<sub>2</sub>RR began to emerge in 2015, although most of them utilized CO<sub>2</sub> reduction as an auxiliary process.

Specifically, in the catalyst design aspect, Shen *et al.* reported the use of a cobalt protoporphyrin molecular catalyst supported on graphite for acidic CO<sub>2</sub>RR at pH values of 1–3 in a one-compartment electrochemical cell in 2015.<sup>66</sup> The results from online electrochemical mass spectrometry demonstrated that the CO<sub>2</sub>RR products, CO and methane, originated from the cobalt protoporphyrin active sites. Also, Ni-doped covalent triazine frameworks were synthesized and utilized to compare CO production on GDE and PE (plate electrode) at the pH

values of 2.0–2.5, showing the superiority of GDE.<sup>67</sup> Additionally, although an alkaline environment is conducive to suppressing the competing HER, some products, such as formic acid, are dissociated in alkaline media, further complicating the separation process. Therefore, acidic CO<sub>2</sub>RR is also advantageous for the downstream separation process. Then, researchers attempted to utilize high pressure to boost the conversion of CO<sub>2</sub> to formic acid in acid. Ramdin *et al.* demonstrated that the FE of formic acid could reach 80% with the assistance of 50 bar pressure at 30 mA cm<sup>-2</sup> in acidic media.<sup>64</sup> Furthermore, there has been research on novel CO<sub>2</sub>RR system designs and the mechanisms among the competing water-reduction HER, proton-reduction HER and CO<sub>2</sub>RR, which were explored under different pH conditions.<sup>68</sup>

During this period, the development of acidic CO<sub>2</sub>RR was accompanied by attempts to design different cells for both performance and mechanism research. Although the number of reports is limited, these studies illustrated the possibility of acidic CO<sub>2</sub>RR operation by designing catalysts and modulating the competitive relationship between CO<sub>2</sub>RR and HER.

### 3.3 Recent resurgence (2020–now)

In recent years, as the detrimental impact of carbon crossover and carbonate formation issues on the practical viability of CO<sub>2</sub>RR under alkaline and neutral conditions became increasingly apparent, the necessity of developing acidic CO<sub>2</sub>RR has been significantly recognized. Meanwhile, given the significant evolution of CO<sub>2</sub>RR reactors and characterization technologies, revisiting acidic CO<sub>2</sub>RR at this stage can potentially lead to further advancements.

Firstly, regarding the transformation of CO<sub>2</sub>RR electrolyzers (Fig. 2b–d), they evolved from two-phase interface reactors to three-phase interface reactors, including conventional H-cells, flow cells, and membrane electrode assemblies (MEA).<sup>69</sup> The traditional two-phase interface reactors include single-chamber reactors and membrane-containing dual-chamber reactors (H-cells). When these two-phase interface reactors are utilized as electrolyzers for CO<sub>2</sub>RR, the solubility of CO<sub>2</sub> in the electrolyte becomes a decisive factor in determining the product selectivity.<sup>9</sup> However, the solubility and diffusion coefficient of CO<sub>2</sub> in acidic electrolyte are limited, resulting in low mass transfer efficiency and slow reaction rates.<sup>69,70</sup> In addition, the distances between the anode and cathode are always large in H-cells, leading to increased internal resistance.<sup>9,69</sup> As a further refinement, flow cells are designed with a porous hydrophobic gas diffusion electrode (GDE), cathode and anode chambers, and an ion exchange membrane. CO<sub>2</sub> can directly contact the GDE layer, allowing the CO<sub>2</sub>RR process to take place at the gas–liquid–solid three-phase interface, largely addressing the issues of low mass transfer efficiency and slow reaction rates.<sup>71</sup> Also, the distance between the anode and cathode is shortened, reducing the resistance of the entire system.<sup>6,9</sup> Although flow-cell electrolyzers are capable of high-current CO<sub>2</sub>RR operation, their stability resulting from the unstable GDE poses a risk of the electrolyte “flooding” issue.<sup>6</sup> The flooding issue originates from the loss of hydrophobicity in the GDE under high-current and long-term operation, causing penetration of the bulk electrolyte into the gas diffusion channels and failure of the CO<sub>2</sub>RR operation. Thus, to alleviate the flooding issue, it is critical to design GDE with exceptional hydrophobicity, porosity and mechanical strength. Operating with no electrolyte passing through the cathode chamber, MEA can partially alleviate the gas diffusion layer blockage and electrolyte flooding issues. Nevertheless, it is likely that the anolyte will diffuse to the cathode side, causing electrolyte flooding. Typically, MEA operating in a two-electrode system retains the high mass transfer efficiency characteristic of the flow cell, enabling a high current density operation. Humid CO<sub>2</sub> passes through GDE and the gas–solid reaction occurs directly. Moreover, compared to flow cells, the shorter anode–cathode distance in MEA further reduces the system impedance, enhancing the reaction rate and energy efficiency. Meanwhile, experimental characterization technologies and theoretical simulation calculation methods for electrocatalytic reactions gradually flourished during this period. Specifically, *in situ* ATR-FTIR and Raman spectroscopy are powerful tools to provide strong evidence for the adsorption of the reaction intermediates and guide the

inference of reaction pathway mechanism.<sup>31,72,73</sup> With the continuous development and widespread adoption of *in situ* electrolyzers, laboratory-level *in situ* characterization has ultimately achieved near-complete simulation of the CO<sub>2</sub>RR reaction environment, broadening the understanding of the reaction interfaces. Furthermore, an increasing number of researchers advocated the combination of experimental work and theoretical calculations; therefore, theoretical calculations have also been adopted for simulating the interfacial adsorption behaviours and reaction pathways.<sup>73,74</sup>

Based on the improvement in CO<sub>2</sub>RR reactors and characterization technologies, the resurgence of acidic CO<sub>2</sub>RR is bound to drive further breakthroughs. In 2021, the first breakthrough came from Huang *et al.*<sup>24</sup> They focused on the interfacial characteristics between the catalyst and the electrolyte, modelling the local pH values at their interface during acidic CO<sub>2</sub>RR under different reduction current densities. Subsequently, they identified the key factor, namely, the cation effect, and leveraged the CO<sub>2</sub> electrostatic stabilization by high-concentration K<sup>+</sup> together with a cation-augmenting layer to induce a local alkaline environment and mitigate the HER competition issue in strongly acidic CO<sub>2</sub>RR. Based on this strategy, high multi-carbon product efficiency (FE<sub>C<sub>2+</sub></sub>, >50%) and SPC (77% at 3.0 sccm) could be achieved in flow cell operation at high current density.<sup>24</sup> Since then, an increasing number of researchers have shifted their focus to acidic CO<sub>2</sub>RR, leading to a surge in catalyst–electrolyte interface engineering research. Specifically, researchers have begun designing various catalyst electric structures for acidic CO<sub>2</sub>RR assisted by high-concentration cation electrolytes to promote the interfacial cation effect and alkalinity.<sup>23,42</sup> Additionally, efforts have also been made to develop methods for acidic CO<sub>2</sub>RR at lower cation concentrations to mitigate the salt crystallization effects.<sup>61,63,75,76</sup> Further, there are also sporadic reports on acidic CO<sub>2</sub>RR in cation-free electrolytes to completely eradicate salt crystallization.<sup>45,47,48</sup> The descriptions of these advancements on acidic CO<sub>2</sub>RR, particularly in catalyst–electrolyte interface engineering, will be categorized and discussed in detail in Section 5.

## 4. Evaluation metrics for acidic CO<sub>2</sub>RR

As emerging technologies advance, an in-depth and precise understanding of their evaluation metrics becomes increasingly important. Numerous direct and indirect evaluation parameters have been reported to assess the electrochemical activity, conversion efficiency, and stability within CO<sub>2</sub>RR reaction systems. Different from the evaluation for neutral and alkaline CO<sub>2</sub>RR, acidic CO<sub>2</sub>RR requires special consideration of the HER competition and local pH-value variation at the reaction interface. Besides, the CO<sub>2</sub> conversion efficiency is generally highlighted as a main advantage of acidic CO<sub>2</sub>RR compared to its neutral and alkaline counterparts. This chapter will explore the special parameters related to acidic CO<sub>2</sub>RR, including methods for detecting H<sup>+</sup> diffusion at the

catalyst–electrolyte interface, localized alkalinity and  $\text{CO}_2$  single-pass conversion efficiency.

#### 4.1 $\text{H}^+$ diffusion

As a fundamental technique, voltammetry, including linear sweep voltammetry (LSV) and cyclic voltammetry (CV), is a common characterization for most electrocatalytic reactions to investigate the catalyst activity, overpotential, the redox transformation process of the catalyst phase, and electrochemically active surface area (ECSA).<sup>55,77</sup> Specially, in this section, LSV, and CV tests will be discussed for assessing the  $\text{H}^+$  diffusion and analysing the competition between HER and  $\text{CO}_2\text{RR}$  in acidic media.

By conducting LSV measurements using a rotating disk electrode (RDE) in different acidic electrolytes or with varying catalysts, typical LSV curves exhibiting an obvious plateau region, followed by a current density increasing region, can be observed.<sup>37,38</sup> The plateau region represents the  $\text{H}^+$  reduction, while the subsequent slope-increasing part corresponds to  $\text{H}_2\text{O}$  reduction.<sup>38</sup> Through RDE-LSV experiments, the diffusion situation of  $\text{H}^+$  during acidic  $\text{CO}_2\text{RR}$  can be revealed. Also, the lowest limiting diffusion current density of  $\text{H}^+$  reduction ( $j_{\text{limit}}$ ) can be calculated using the Levich equation, as follows:<sup>38</sup>

$$j_{\text{limit}} = -0.62nFAD_{\text{H}^+}^{2/3}\omega^{1/2}\nu^{-1/6}c_{\text{H}^+} \quad (4.1)$$

where  $n$  is the electron transfer number in the half reaction,  $F$  is the Faraday constant,  $A$  is the electrode area,  $\omega$  is the RDE

rotating speed ( $\text{rad s}^{-1}$ ),  $\nu$  is the kinematic viscosity of water ( $1.0 \times 10^{-6} \text{ m}^2 \text{ s}^{-1}$ ), and  $D_{\text{H}^+}$  is the  $\text{H}^+$  diffusion coefficient in water. As an application, research demonstrated that with an increase in the alkali-cation concentration in the electrolyte, the current density for  $\text{H}^+$  reduction, namely the plateau region, decreases and gradually approaches the  $j_{\text{limit}}$  value (Fig. 3a). This result demonstrates that a high concentration of alkali cations suppresses the  $\text{H}^+$  mass transfer and competing HER during acidic  $\text{CO}_2\text{RR}$ .<sup>38,68,78</sup> Empirically, this method can be extended to more electrolyte modification systems as an evaluation indicator and a factor for predicting the performance for acidic  $\text{CO}_2\text{RR}$ .

As an extended application, the transformed form of the Levich equation can be utilized to compare the  $D_{\text{H}^+}$  values based on different catalysts in the same electrolyte formula and highlight the positive influence of catalyst engineering for acidic  $\text{CO}_2\text{RR}$  on suppressing the competing HER. Specifically, the CV curves of different electrocatalysts in a certain electrolyte can be obtained by RDE experiments at different rotation rates (Fig. 3b). Further, the ratio of the  $\text{H}^+$  diffusion coefficients ( $D_{\text{H}^+}$ ) of the experimental group to the control group can be calculated using the following equation:<sup>63</sup>

$$\frac{D_{\text{experiment}}}{D_{\text{control}}} = \left( \frac{j_{\text{experiment}}/\omega_{\text{experimental}}^{1/2}}{j_{\text{control}}/\omega_{\text{control}}^{1/2}} \right)^{3/2} \quad (4.2)$$

Thus, after linearly fitting the plateau current ( $j$ ) against the square root of the RDE rotation rate ( $\omega^{1/2}$ ), the ratio of  $D_{\text{H}^+}$

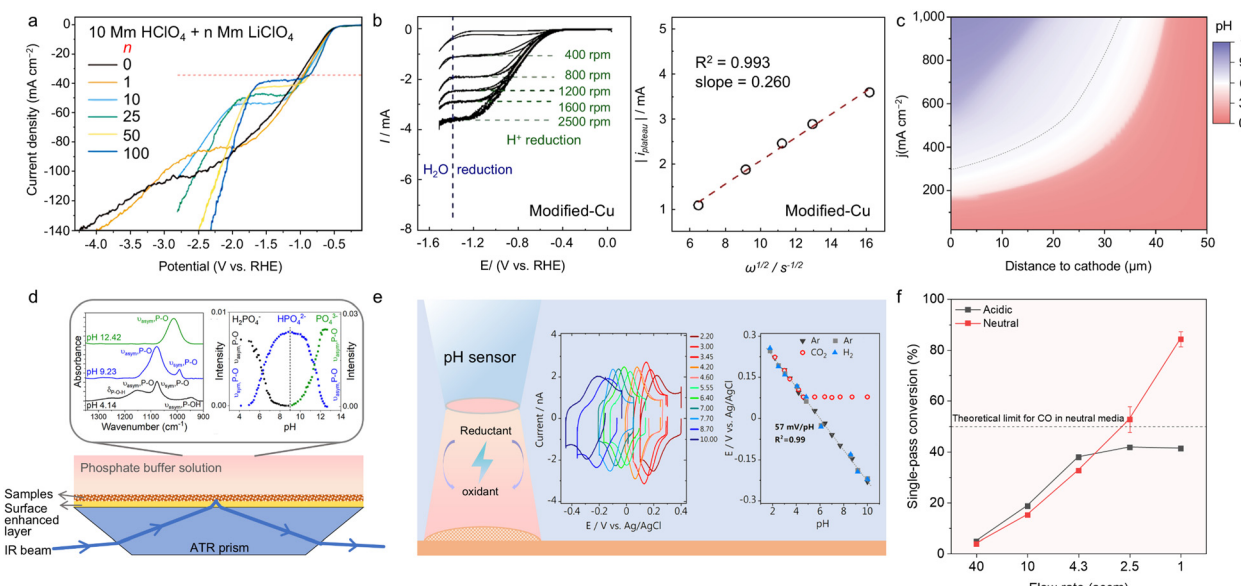


Fig. 3 (a) LSV curves of Au RDE in Ar-saturated acidic electrolytes with different concentrations of  $\text{Li}^+$ . The red dashed line represents the limiting diffusion current density of  $\text{H}^+$  reduction using the Levich equation.<sup>38</sup> Reproduced with permission from ref. 38. Copyright 2023, the American Chemical Society. (b) CV curves of modified-Cu RDE in  $\text{N}_2$ -saturated 0.1 M  $\text{KClO}_4/\text{HClO}_4$  solutions at different rotation rates and linear fitting of  $i_{\text{plateau}}$  vs.  $\omega^{1/2}$  for modified-Cu RDE based on Levich equation.<sup>63</sup> Reproduced with permission from ref. 63. Copyright 2023, Wiley-VCH. (c) pH modelling results at different current densities and cathode distances in 1 M  $\text{H}_3\text{PO}_4$  and 3 M  $\text{KCl}$ .<sup>24</sup> Reproduced with permission from ref. 24. Copyright 2021, the American Association for the Advancement of Science. (d) Schematic of working mechanism of ATR-SEIRA, SEIRA spectra of phosphate standard solutions, and the corresponding calibration curves.<sup>79</sup> (e) Schematic of working mechanism of SECM, voltammetry curves of pH sensor in different pH-based  $\text{Li}_2\text{SO}_4$  standard solutions, and corresponding calibration curves.<sup>80</sup> (f) SPCE comparison of Ag/PTFE under acidic and neutral conditions.<sup>81</sup> Reproduced with permission from ref. 81. Copyright 2022, the American Chemical Society.

values can be obtained and the  $H^+$  mass transfer near the electrode interface induced by different catalysts can be compared.<sup>37,63</sup>

Furthermore, it is worth noting that the voltage loss due to the electrolyte between the working and reference electrode should be considered and corrected using *iR* compensation in the analysis of the CV and LSV results.<sup>82</sup> Simultaneously, the scan rate also significantly impacts CV and LSV measurements, and thus maintaining a consistent scan rate is crucial for effectively controlling the variables in comparisons.<sup>83</sup>

#### 4.2 Interfacial pH

To date, the importance of interfacial properties is increasingly emphasized in  $CO_2$ RR, and thus methods for the characterization of interfaces have continuously diversified through the dedicated efforts by researchers. As mentioned before, interfacial alkalinity is a key parameter to predict the potential  $CO_2$ RR performance in acidic media, which can affect the reaction selectivity, efficiency and product distributions. Monitoring the local pH value allows researchers to deeply understand the reaction environment at the catalyst-electrolyte interfaces. However, unlike the bulk pH level, directly measuring the interfacial pH value is challenging, making it necessary to rely on other methods for assistance. To date, various techniques have been developed to monitor the interfacial pH indirectly, including theoretical calculation modelling, *in situ* spectroscopy (FTIR and Raman), fluorescent probes and electrochemical measurements.

As a crucial breakthrough of acidic  $CO_2$ RR, Huang *et al.* pioneered the investigation of the interfacial pH levels on the catalyst interfaces, examining how the pH level changes with variations in the operating current density and distances to the cathode through theoretical modelling.<sup>24</sup> Specifically, they employed the COMSOL Multiphysics software to account for all the species interactions within the phosphate buffer electrolytes ( $CO_2$ ,  $HCO_3^-$ ,  $CO_3^{2-}$ ,  $H_3PO_4$ ,  $H_2PO_4^-$ ,  $HPO_4^{2-}$ ,  $PO_4^{3-}$ ,  $OH^-$ ,  $H^+$  and  $H_2O$ ). Also, the model incorporated all homogeneous and heterogeneous reactions throughout the system. The concentrations and pH levels of the bulk electrolytes were identified by experiments and applied to the model. Additionally, the thickness of the diffusion layer, porosity and catalyst length were set as fixed parameters. After setting the boundary conditions of the model, the local pH values were calculated at different current densities, revealing the pH variation trend on the catalyst-electrolyte interface. The results indicated that in the bulk electrolyte with a pH of 1, the interfacial pH (distance to cathode was 0  $\mu m$ ) is almost similar to that in the bulk solution, and the interfacial pH level increases to neutrality and even alkalinity as the current density increases (Fig. 3c). This effect originates from the local rate of the  $H^+$  consumption exceeding the  $H^+$  mass transfer rate from the bulk. However, the pH level can reduce to acid within the cathodic distance of 50  $\mu m$ , avoiding  $CO_2$  loss and carbon crossover to the anolyte.

Further, *in situ* spectroscopy (ATR-FTIR and Raman) has also been applied to investigate the surface pH changes during the

acidic  $CO_2$ RR process.<sup>79</sup> Specifically, to enhance the signal intensity and sensitivity, surface-enhanced techniques for both ATR-FTIR and Raman spectroscopy, named attenuated total reflection surface-enhanced infrared adsorption spectroscopy (ATR-SEIRAS) and surface-enhanced Raman spectroscopy (SERS), are implemented by coating a polycrystalline Ag/Au underlayer on the cathode substrate (Fig. 3d).<sup>10,79,84</sup> During the pH detection process, a phosphate buffer solution serves as an indicator of the pH variation. Firstly, it is necessary to record the spectra of the phosphate species ( $H_2PO_4^-$ ,  $HPO_4^{2-}$ , and  $PO_4^{3-}$ ) within different pH-value phosphate standard solutions, creating a calibration spectrum. After peak deconvolution, the peak intensities attributed to  $H_2PO_4^-$ ,  $HPO_4^{2-}$ , and  $PO_4^{3-}$  can be identified and plotted as a function of pH value to generate a calibration curve (Fig. 3d, inset). In the case of experimental samples, it is necessary to detect the ATR-SEIRAS or SERS spectra and calculate the intensity of the phosphate-related peaks. Subsequently, the interfacial pH is estimated by matching the peak intensities to the calibration curve. It should be noted that in neutral and alkaline systems, carbonate species can also act as a local pH indicator; however, carbonates are unstable in acid media, and thus phosphate species are more suitable for monitoring the interfacial pH in the acidic  $CO_2$ RR.

Fluorescence confocal laser scanning microscopy (CLSM) measurement has been extended to monitor the interfacial pH during acidic  $CO_2$ RR.<sup>79</sup> After selecting an appropriate fluorescent probe that is sensitive to the required pH range, the probe is dissolved in standard solutions with varying pH values. Subsequently, the probe is excited by lasers at two different wavelengths. By collecting the fluorescence emission from both excitations, the resulting emission ratios serve as pH indicators, which can be plotted against pH value to create a calibration curve. Similarly, to characterize the interfacial pH in acidic  $CO_2$ RR, fluorescent probes are deposited on the  $CO_2$ RR cathode, and adsorption spectra are acquired during the acidic  $CO_2$ RR process. Finally, the emission ratio is calculated and compared with the calibration curve to determine the interfacial pH level.

Also, electrochemical signals can also be applied as a response to interfacial pH level. Under mass transport control, the local pH level changes during  $CO_2$ RR can be measured using the rotating ring-disk electrode (RRDE) technique, with an Au disk and Pt ring electrode.<sup>85</sup> In this method, the  $CO_2$ RR product, CO molecule, serves as the probe, which can be generated at the Au disk during the  $CO_2$ RR process, and then oxidized into  $CO_2$  on the Pt ring electrode by CO oxidation. The oxidation of CO at the Pt ring electrode causes a pH-sensitive peak shift, which can be used to track the local pH changes. To measure the local pH values, the CV curves are first recorded in standard solutions with known pH values. A calibration curve can be created based on the correlation between the known solution pH and CO oxidation peak potential. By matching the measured CO oxidation peak potential in experimental acidic  $CO_2$ RR systems, the interfacial pH can be estimated. Scanning electrochemical microscopy (SECM) based on electrochemical

mechanisms can drive the microelectrode to scan the sample interface and detect current variations induced by the oxidation and reduction of substances within the micro-zone. With advancements in SCEM technology, it has been utilized as a high-resolution tool for local pH measurements in CO<sub>2</sub>RR, using specialized pH-sensitive probes (Fig. 3e).<sup>80,86</sup> Typically, the probes consist of redox species with distinct oxidation and reduction peaks observable in CV tests, where the mid-peak potentials shift in response to the pH changes. Thus, a calibration curve can be constructed by correlating the pH values and their corresponding mid-peak potentials, and the interfacial pH of the experimental systems can be determined.

In summary, advances in characterization techniques have driven a deeper understanding of electrocatalytic reactions. As the importance of creating surface alkaline microenvironments continues to be emphasized in acidic CO<sub>2</sub>RR, more interfacial pH measurement methods have been developed, certainly driving further progress in catalyst–electrolyte engineering.

#### 4.3 CO<sub>2</sub> single-pass conversion efficiency

When evaluating the efficiency of CO<sub>2</sub>RR, three key dimensions are involved, *i.e.*, electron transfer, electricity consumption, and carbon conversion, which correspond to the faradaic efficiency (FE), energy efficiency (EE), and CO<sub>2</sub> single-pass conversion efficiency (SPCE), respectively. As the most common metrics of product selectivity and electricity cost for CO<sub>2</sub>RR, FE and EE are used to evaluate CO<sub>2</sub>RR across all pH levels, respectively. SPCE, defined as the ratio of the carbon content in the CO<sub>2</sub>RR products to the total input CO<sub>2</sub>, serves as a measure of the carbon utilization efficiency.<sup>25</sup> Due to the generation of carbonate and the subsequent carbon crossover phenomenon, the input CO<sub>2</sub> gas in neutral and alkaline media is mostly transferred to the anode side, and theoretically the SPCE is typically lower in alkaline and neutral CO<sub>2</sub>RR, which is less than 50% for C<sub>1</sub> products and below 25% for C<sub>2+</sub> products.<sup>41,81</sup> Thus, in most reported works on alkaline and neutral CO<sub>2</sub>RR, SPCE is rarely discussed. In contrast, carbon crossover is significantly reduced in acidic media, and the SPCE values are more widely discussed in acidic CO<sub>2</sub>RR studies, with values up to 90% achieved (Fig. 3f).<sup>81</sup>

The SPCE can be calculated using the following equation:

$$\text{SPCE (\%)} = \frac{\text{consumed CO}_2}{\text{input CO}_2} \times 100$$

$$= \frac{60 \times I \times x \times \text{FE}}{N \times F \times v_{\text{input}} \times 1 \text{ min} \div V_m} \times 100 \quad (4.3)$$

where  $I$  represents operation current of the reaction,  $x$  is the mole ratio of CO<sub>2</sub> for a specific product ( $x_i = 1$  for C<sub>1</sub> products and  $x_i = 2$  for C<sub>2</sub> products), FE is the faradaic efficiency of a certain product,  $N$  represents the mole number of electrons for one molecule of a certain product,  $F$  is the Faraday constant,  $v_{\text{input}}$  is the experimental input CO<sub>2</sub> flow rate, and  $V_m$  is the gas molar volume.

## 5. Catalyst–electrolyte interface engineering for promoting acidic CO<sub>2</sub> electroreduction

Recently, an increasing number of strategies have been proposed to promote CO<sub>2</sub>RR-related intermediate adsorption and enhance the performance of acidic CO<sub>2</sub>RR. In general, these strategies revolve around catalyst–electrolyte engineering and can be categorized into three main approaches, catalyst modification, electrolyte engineering and interface optimization (Fig. 4). In this chapter, we summarize these modification strategies and highlight the recent advancements in this field.

### 5.1 Electrolyte engineering

In the CO<sub>2</sub> electroreduction reaction, the electrolyte directly interacts with the electrocatalyst, significantly affecting the overall reaction environment, the distribution of active sites and the reaction efficiency. Thus, a thorough investigation of the electrolyte properties, including its pH level, composition and concentration, is meaningful for understanding and optimizing the reaction process. Building on the comprehensive understanding of the influence of electrolyte pH level, composition and cation concentration on acidic CO<sub>2</sub>RR processes, some studies have been dedicated to integrating additives into acidic electrolytes, reconstructing the electrolyte structure and driving a CO<sub>2</sub>RR-promoted interface in acid media. The aforementioned methods are all involved in electrolyte engineering, which involves deliberate modification of the electrolyte properties to effectively optimize the reaction microenvironment, promote the adsorption of CO<sub>2</sub>RR-related intermediates, and ultimately enhance the CO<sub>2</sub>RR performance in acidic media. Different from pure electrolyte engineering, electrolyte engineering at the interface specifically influences the cathodic region within the electrical double layer during the acidic CO<sub>2</sub>RR process, impacting the ion transport, local pH and intermediate adsorption.<sup>87</sup> In this section, electrolyte engineering at the interface will be discussed according to the cation effect, hydrogen bond (H-bond) reconstruction and maintaining the high valence of catalysts. The reported acidic CO<sub>2</sub>RR performance driven by electrolyte engineering is summarized in Table 1.

**5.1.1 Cation effect.** As previously mentioned, although conducting the CO<sub>2</sub> electroreduction reaction in an acidic environment is an ideal countermeasure for addressing the carbonate crossover issues, it is highly challenging to perform CO<sub>2</sub> reduction in pure acidic electrolytes, given that it is completely hindered by the competing HER. Interestingly, it has been discovered that cation species in the acidic electrolyte can suppress the HER and enhance the performance of the acidic CO<sub>2</sub>RR.<sup>26</sup> As illustrated in Fig. 5a, it is acknowledged that alkali-metal cations are solvated with the free water molecules in the electrolyte, forming a stable solvation shell. This interaction alters the structure of the interfacial water molecules, diminishes the activity of H<sup>+</sup> and decreases the availability of water molecules as proton donors. Additionally, high

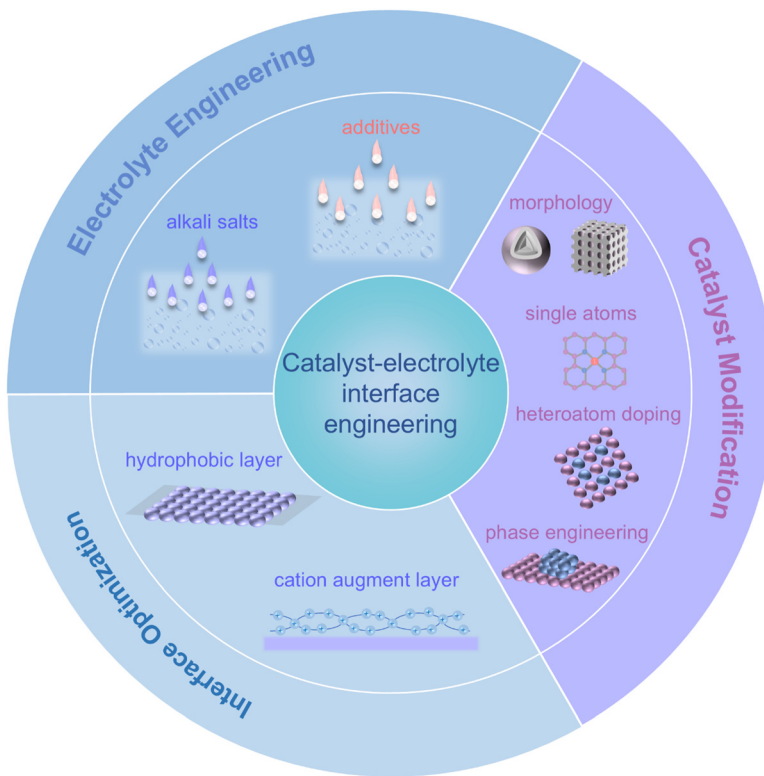


Fig. 4 Schematic of catalyst–electrolyte interface engineering strategies for promoting acidic CO<sub>2</sub>RRs.

Table 1 Acidic CO<sub>2</sub>RR performance driven by electrolyte engineering

Category	Catalyst	Electrolyte	Main products	FE	SPCE	Stability (h)	Ref.
Cation effect	Cu catalyst	1 M H <sub>3</sub> PO <sub>4</sub> + 3 M KCl (pH < 1)	CH <sub>4</sub>	28% (400 mA cm <sup>-2</sup> )	—	—	24
	Bi nanosheet	0.05 M H <sub>2</sub> SO <sub>4</sub> + 3 M KCl (pH < 1)	HCOOH	92.2% (257 mA cm <sup>-2</sup> )	27.4% (3 sccm)	8	59
	Ni–N–C catalyst	0.5 M K <sub>2</sub> SO <sub>4</sub> + H <sub>2</sub> SO <sub>4</sub> (pH = 0.5)	CO	95% (500 mA cm <sup>-2</sup> )	—	8	76
	Ag/PTFE	0.01 M H <sub>2</sub> SO <sub>4</sub> + 0.01 M Cs <sub>2</sub> SO <sub>4</sub> (pH ≤ 3)	CO	80% (60 mA cm <sup>-2</sup> )	90% (1 sccm)	50	81
	10 cm <sup>2</sup> Au GDE	1 M Cs <sub>2</sub> SO <sub>4</sub> (pH = 2–4)	CO	80–90% (200 mA cm <sup>-2</sup> )	—	—	88
	Cu–PTFE	Na <sub>2</sub> SO <sub>4</sub> + H <sub>2</sub> SO <sub>4</sub> (pH = 2)	CH <sub>4</sub>	48% (220 mA cm <sup>-2</sup> )	—	—	89
	Cu–PTFE	Na <sub>2</sub> SO <sub>4</sub> + K <sub>2</sub> SO <sub>4</sub> + H <sub>2</sub> SO <sub>4</sub> (pH = 2; Na <sup>+</sup> /K <sup>+</sup> ratio is 1 : 1)	C <sub>2+</sub>	46% (220 mA cm <sup>-2</sup> )	—	—	89
	Cu–PTFE	K <sub>2</sub> SO <sub>4</sub> + H <sub>2</sub> SO <sub>4</sub> (pH = 2)	C <sub>2+</sub>	70% (220 mA cm <sup>-2</sup> )	—	—	89
Reconstruction of H-bonds	Ag catalyst	0.1 M H <sub>2</sub> SO <sub>4</sub> + 0.4 M K <sub>2</sub> SO <sub>4</sub> + 0.1 M SPS (pH ≈ 1.42)	CO	97.8% (250 mA cm <sup>-2</sup> )	66.3% (2 sccm)	20	90
	Ag powder	0.1 M H <sub>2</sub> SO <sub>4</sub> + 0.2 M K <sub>2</sub> SO <sub>4</sub> + 2 wt% PSS (pH ≈ 1.42)	CO	93.9% (250 mA cm <sup>-2</sup> )	72.2% (2 sccm)	12	91
Maintaining the high valence of catalysts	Cu particles	0.3 M KI + 0.05 M H <sub>2</sub> SO <sub>4</sub> + 20 mM I <sub>2</sub> (pH = 1.2)	C <sub>2+</sub>	70% (600 mA cm <sup>-2</sup> )	54% (2.5 sccm)	8	75

concentrations of cations accumulating at the reaction interface can shield the H<sup>+</sup> near the electrode surface and elevate the localized pH level, which can buffer the acidic environment. This prevents the diffusion of H<sup>+</sup> towards the electrode interface, inhibiting the HER competition and enhancing the CO<sub>2</sub>RR selectivity. Huang *et al.* explored this by using high-concentration phosphate buffer solutions as the base acidic

electrolyte and adjusting the electrolyte composition by adding various concentrations of KCl.<sup>24</sup> Combining the interface modelling and Tafel analysis results, it was found that the surface pH increased and even approached alkaline levels at high current densities and the cations reinforced the ability of the surface to activate CO<sub>2</sub> and suppress HER. Taking advantage of this cation promotion effect, the selectivity for CH<sub>4</sub> of 28% was

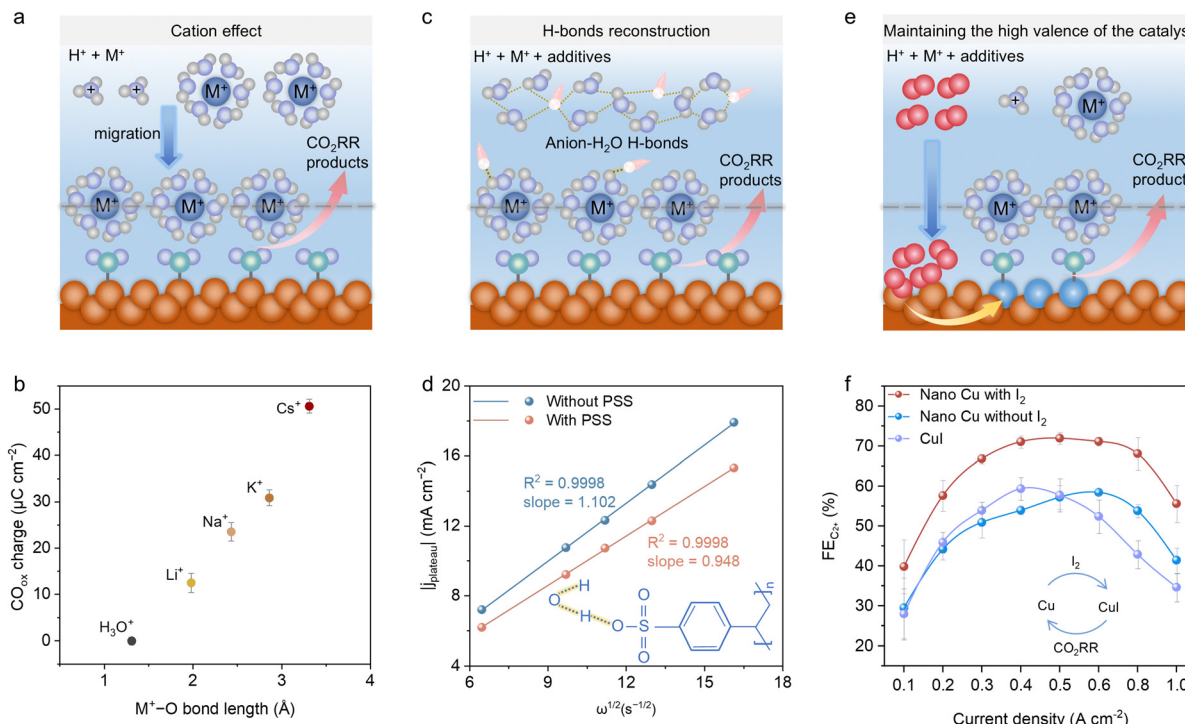


Fig. 5 (a) Illustration of the cation effect on acidic CO<sub>2</sub>RRs with alkali metal salts. (b) Correlation between cation–water radial distribution (M<sup>+</sup>–O bond length) and acidic CO<sub>2</sub>RR production.<sup>36</sup> Reproduced with permission from ref. 36. Copyright 2021, Springer Nature. (c) Illustration of H-bond reconstruction in acidic CO<sub>2</sub>RR electrolytes by additives. (d) Comparison of H<sup>+</sup> diffusion coefficients of electrolytes with/without PSS, which can break the H-bond network of water molecules.<sup>91</sup> Reproduced with permission from ref. 91. Copyright 2024, Wiley-VCH. (e) Illustration of the high-valent catalyst maintaining effect by special oxidant additives. (f) Comparison of FE<sub>C<sub>2</sub>+</sub> of acidic CO<sub>2</sub>RR reaction systems among nano-Cu with I<sub>2</sub>, nano-Cu without I<sub>2</sub>, and Cul without I<sub>2</sub>, showing the oxidation effect of I<sub>2</sub> on the acidic CO<sub>2</sub>RR performance.<sup>75</sup> Reproduced with permission from ref. 75. Copyright 2024, the American Chemical Society.

achieved in 1 M KCl-added phosphate solutions on Cu catalysts at 400 mA cm<sup>-2</sup>. Additionally, the selectivity for the CO<sub>2</sub>RR products increased as the cation concentration increased. Similarly, Bi nanosheets were synthesized to investigate the K<sup>+</sup>-assisted effect on acidic CO<sub>2</sub>RR for the production of formic acid.<sup>59</sup> The results showed that the introduction of KCl effectively suppressed HER and the FE for formic acid was directly proportional to the salt concentration. As an efficient CO<sub>2</sub>RR electrocatalyst for CO production, Ni-N-C was utilized as a model to probe the cation promotion effect under acidic MEA electrolysis, demonstrating that both the CO FE and the full-cell energy efficiency largely decreased with a decrease in the K<sup>+</sup> concentration.<sup>76</sup> Further, research indicates that maintaining a K<sup>+</sup> concentration of above 2.0 M is advantageous for Cu-based catalysts to achieve a competitive C<sub>2</sub><sup>+</sup> product FE (>60%).<sup>23,25</sup>

Moreover, it has been recognized that under alkaline conditions, the electrolyte composition, namely alkali cation (Li<sup>+</sup>, Na<sup>+</sup>, K<sup>+</sup> and Cs<sup>+</sup>), influences the CO<sub>2</sub>RR performances, following the order of Cs<sup>+</sup> > K<sup>+</sup> > Na<sup>+</sup> > Li<sup>+</sup>.<sup>92,93</sup> Therefore, it is worthwhile to analyse and compare the trend in the variation of CO<sub>2</sub>RR product selectivity in different alkali-cation electrolytes under acidic condition as well. Gu *et al.* investigated acidic CO<sub>2</sub>RR using electrolytes composed of 0.1 M HOTf + 0.4 M MOTf (M = Li, Na, K, and Cs) with both SnO<sub>2</sub>/C and Cu/C catalysts, exhibiting that all the alkali cations enhanced CO<sub>2</sub>RR

by suppressing HER, with the selectivity following the order of Li<sup>+</sup> < Na<sup>+</sup> < K<sup>+</sup> < Cs<sup>+</sup> on SnO<sub>2</sub>/C and Li<sup>+</sup> < Na<sup>+</sup> < K<sup>+</sup> ≈ Cs<sup>+</sup> on Cu/C.<sup>37</sup> Also, the mechanistic study revealed that hydrated alkali cations (M<sup>+</sup>–H<sub>2</sub>O) and H<sub>3</sub>O<sup>+</sup> competed for adsorption at the outer Helmholtz plane (OHP) at the cathode side. Promptly, a chemically inert layer of alkali cations formed at the OHP, shielding the cathodic electric field over an extended potential range, which restricted the movement of H<sub>3</sub>O<sup>+</sup> ions. Without alkali cations, the migration of H<sub>3</sub>O<sup>+</sup> under the influence of an electric field accelerates their replenishment at the outer Helmholtz plane, thereby initiating HER. Besides, Pan *et al.* utilized an acid-fed MEA with Ag catalysts and observed an increase in CO FE from 8% to 77% at 60 mA cm<sup>-2</sup>, following the cation sequence of H<sup>+</sup> < Li<sup>+</sup> < Na<sup>+</sup> ≈ K<sup>+</sup> ≤ Cs<sup>+</sup> in a mild acid electrolyte.<sup>81</sup> A CO FE of 80% and SPCE of 90% could be achieved at 60 mA cm<sup>-2</sup> in 0.01 M H<sub>2</sub>SO<sub>4</sub> + 0.01 M Cs<sub>2</sub>SO<sub>4</sub> electrolyte with a stability of 50 h. The feasibility of the cation promotion effect was further evaluated using practical electrode geometries with a 10 cm<sup>2</sup> gold electrode. The results suggest that the FE for CO can reach 80% at current densities ranging from 50 to 200 mA cm<sup>-2</sup> in 1 M CsSO<sub>4</sub> electrolyte at pH values of 2, 3, and 4. In contrast, when using 1 M Li<sub>2</sub>SO<sub>4</sub>, almost no CO product was produced at all the applied current densities.<sup>88</sup> As an interesting attempt, Xu *et al.* modified an acidic electrolyte by adjusting the concentration ratio of K<sup>+</sup> and

$\text{Na}^+$ , discovering that this ratio can influence the product distribution on the Cu-based catalyst.<sup>89</sup> Specifically, in an electrolyte containing only  $\text{Na}^+$ ,  $\text{CH}_4$  was the dominant product, achieving an FE of 48%, together with an FE of 39% for  $\text{H}_2$ . With the gradual addition of  $\text{K}^+$ , the FE for  $\text{CH}_4$  and  $\text{H}_2$  progressively decreased, while the selectivity for  $\text{C}_{2+}$  products increased. Ultimately, when the electrolyte was adjusted to only contain  $\text{K}^+$  cations, the FE for the  $\text{C}_{2+}$  products reached 70%. These findings indicate that the type of alkali metal cation in the acidic electrolyte can directly influence the  $\text{CO}_2\text{RR}$  product distribution, warranting a deeper investigation into the underlying mechanisms. Monteiro *et al.* applied CV measurements of  $\text{CO}_2$  reduction and CO oxidation on Au catalysts in different cation composition electrolytes to quantify the CO production during acidic  $\text{CO}_2\text{RR}$ .<sup>36</sup> The results suggested that the CO production was correlated with the size of the solvated cations following the order of  $\text{Li}^+ < \text{Na}^+ < \text{K}^+ < \text{Cs}^+$  (Fig. 5b). Based on the experimental results, *ab initio* molecular dynamics (AIMD) simulations were carried out using an alkali metal cation-inserted Au model ( $\text{Au}-\text{H}_2\text{O}-\text{M}^+$ ). The calculation result indicated that a larger cation ionic radius corresponded to a softer solvation shell and the average cation coordination number was determined to be 2.8, 3.2, 3.5 and 5.8 for  $\text{Li}^+$ ,  $\text{Na}^+$ ,  $\text{K}^+$  and  $\text{Cs}^+$ , respectively. Additionally,  $\text{Li}^+$  exhibited a limited  $\text{CO}_2$  coordination number due to its hard solvation shell; meanwhile, other alkali metal cations can continuously bind to the oxygen atoms in  $\text{CO}_2$  and the coordination number followed the order of  $\text{Li}^+ < \text{Na}^+ < \text{K}^+ < \text{Cs}^+$ . Also, it was concluded that the  $\text{CO}_2\text{RR}$  activity trend depends on the cation surface concentrations at the OHP and the differing ability of cations to coordinate with the  $^*\text{CO}_2^-$  intermediate, ranging from minimal bonding for  $\text{Li}^+$  to double bonds for  $\text{Cs}^+$ . This cation effect topic was further expanded to multivalent cations ( $\text{Li}^+$ ,  $\text{Cs}^+$ ,  $\text{Be}^{2+}$ ,  $\text{Mg}^{2+}$ ,  $\text{Ca}^{2+}$ ,  $\text{Ba}^{2+}$ ,  $\text{Al}^{3+}$ ,  $\text{Nd}^{3+}$ , and  $\text{Ce}^{3+}$ ) in acidic electrolyte at pH 3.<sup>94</sup> It was found that cations with soft hydration shells ( $\text{Cs}^+$ ,  $\text{Ba}^{2+}$ , and  $\text{Nd}^{3+}$ ) exhibited minimal cation–cation repulsion, allowing them to effectively accumulate at OHP and coordinate with  $^*\text{CO}_2^-$ . However, trivalent cations can enhance both  $\text{CO}_2\text{RR}$  and water dissociation. Thus,  $\text{Nd}^{3+}$  can only activate  $\text{CO}_2\text{RR}$  at the potential range below  $\text{H}_2\text{O}$  reduction, while  $\text{Cs}^+$  and  $\text{Ba}^{2+}$  can promote  $\text{CO}_2\text{RR}$  at higher overpotentials. Furthermore, the Levich equation was applied to investigate the cation effect on suppressing the mass transport of  $\text{H}^+$  reduction during acidic  $\text{CO}_2\text{RR}$ .<sup>38</sup> Following LSV tests of Au RDE in  $\text{HClO}_4$  acidic electrolyte with different  $\text{LiClO}_4$  concentrations, the current density for  $\text{H}^+$  reduction in the plateau region decreased with an increase in the cation concentration, and gradually approached the limiting diffusion current density for  $\text{H}^+$  reduction. To more intuitively observe the impact of different concentrations and types of cations in the electrolyte on the acidic  $\text{CO}_2\text{RR}$  process, ATR-SEIRAS was applied to reveal the differences in the intermediate adsorption.<sup>95</sup> Firstly, the *in situ* ATR-SEIRAS tests were conducted on a Cu film in both 0.05 M  $\text{H}_2\text{SO}_4$  and 0.05 M  $\text{H}_2\text{SO}_4/1\text{ M Na}_2\text{SO}_4$ . The results showed that adsorption peaks appeared at 2056, 1466 and 1416  $\text{cm}^{-1}$  during different potential reduction processes, which can be assigned

to atop-bound CO, asymmetry stretching of adsorbed  $\text{CO}_2$  and bidentate  $\text{COO}^-$ , respectively. Subsequently, the cation effect was quantified by comparing the peak intensity of adsorbed  $\text{CO}_2$  at 1466  $\text{cm}^{-1}$  in acidic electrolytes containing differing cations. Combining AIMD simulations and the spectroscopic features of water, the findings indicated that the  $\text{CO}_2$  adsorption in the Li-based electrolyte was more efficient than that with other cations. Nevertheless, the hard hydrated shell of  $\text{Li}^+$  impeded hydrogen atoms from approaching the oxygen atoms in the adsorbed  $\text{CO}_2$ , decelerating the further hydrogenation of  $\text{CO}_2$ . On the contrary, larger cations possessed much softer hydration shells, facilitating the interaction of hydrogen atoms and  $\text{CO}_2$  and leading to more effective  $\text{CO}_2\text{RR}$ .<sup>95</sup>

Briefly, the internal mechanism of the cation promotion effect may originate from three viewpoints, as follows: (1) adjustment of the electronic field near the OHP; (2) activating and stabilizing the  $\text{CO}_2\text{RR}$  intermediate by coordination and (3) regulating the local pH level. Besides the cation effect, it is worth exploring the anion impact on acidic  $\text{CO}_2\text{RR}$  processes. Research shows that most anions have an insignificant influence on the  $\text{CO}_2\text{RR}$ , referring to the negligible production distribution differences by substituting  $\text{SO}_4^{2-}$  with  $\text{I}^-$ ,  $\text{Cl}^-$  and  $\text{Br}^-$ .<sup>24,59</sup> However, if special anion chemisorption occurs on the catalyst surface, the electronic structure of catalysts can be optimized, favouring the  $\text{CO}_2\text{RR}$  kinetics.<sup>96,97</sup> Also, anions with buffering ability can influence the local pH on the cathode surface, modifying the product distribution.<sup>98</sup>

**5.1.2 H-bond reconstruction.** Based on the findings regarding the alkali cation effect, some studies have been devoted to further promoting acidic  $\text{CO}_2\text{RR}$  by introducing additives with special properties into acidic electrolytes. As shown in Fig. 5c, certain additives interact with  $\text{H}_2\text{O}$  molecules and disrupt the original H-bond network among  $\text{H}_2\text{O}$  through coordination and electrostatic interactions with  $\text{H}_2\text{O}$ , reducing the aggregability of water molecules and the activity of  $\text{H}^+$ , thereby, suppressing the competing HER. Meanwhile, owing to their highly electronegative atoms, these additives can act as H-bond acceptors, forming new H-bond structures with the donor hydrogen atoms in  $\text{H}_2\text{O}$ , optimizing the interfacial reaction environment and enhancing the intermediate stability and  $\text{CO}_2\text{RR}$  selectivity. Inspired by the H-bond environment modulation ability of sulfonate-based molecules, Ge *et al.* utilized a series of sulfonate-based molecules, *i.e.*, sodium *p*-styrenesulfonate (SPS), sodium *p*-toluene sulfonate (STS), and sodium benzene-sulfonate (SBS), as electrolyte additives to enhance the acidic  $\text{CO}_2\text{RR}$  performance.<sup>90</sup> Raman and  $^1\text{H}$  NMR spectroscopy revealed that the H-bond interaction ability between additives and water followed the order of SPS > STS > SBS and the decreasing magnitude of HER activity followed the same order. Therefore, as the most effective additive, the SPS-added system enabled a high CO FE of 97.8% and an SPCE of 66.3% at 250  $\text{mA cm}^{-2}$  using commercial Ag catalysts in 0.1 M  $\text{H}_2\text{SO}_4$  + 0.4 M  $\text{K}_2\text{SO}_4$  + 0.1 M SPS electrolyte. This result confirms that introducing sulfonate-based molecules can hinder proton transfer and reduce the proton concentration at the catalyst–electrolyte interface, suppressing the HER and boosting  $\text{CO}_2\text{RR}$ .

Similarly, polystyrene sulfonate (PSS), which can reshape the interfacial H-bond network, was also employed as an electrolyte additive for acidic CO<sub>2</sub>RR.<sup>91</sup> According to <sup>39</sup>K nuclear magnetic resonance (NMR) spectroscopy, zeta potential, and inductively coupled plasma optical emission spectroscopy measurements, the addition of PSS influenced the K<sup>+</sup> solvation structure and drove a high-concentration K<sup>+</sup> interface. Additionally, the RDE-CV experiments and calculations based on the Levich equation confirmed that with the addition of PSS, the proton diffusion coefficient decreased by 20.2% compared to that without PSS (Fig. 5d). As a result, a CO FE of 93.9% at 250 mA cm<sup>-2</sup> on the Ag catalyst could be achieved in the acidic medium of 0.1 M H<sub>2</sub>SO<sub>4</sub> + 0.2 M K<sub>2</sub>SO<sub>4</sub> with 2 wt% PSS.

**5.1.3 Maintaining the high valence of catalysts.** The valence state is essential in determining the electrocatalytic activity, reaction selectivity and stability of electrocatalysts. In terms of CO<sub>2</sub>RR, Cu-based catalysts are widely used for the high-efficiency production of multi-carbon products (C<sub>2+</sub>), and the product distribution is generally diverse depending on the Cu valence state. Typically, Cu<sup>(II)</sup> is considered to facilitate CH<sub>4</sub> production, while Cu<sup>(I)</sup> together with Cu<sup>0</sup> can induce a synergistic effect to promote C-C coupling and achieve high C<sub>2+</sub> product selectivity.<sup>74,99</sup> Acidic CO<sub>2</sub>RR with high carbon utilization efficiency encounters challenges in terms of limited C-C coupling ability. However, high alkali-cation concentrations, the main solution in reported studies, will induce salt crystallization and block the CO<sub>2</sub> transport channels. Thus, modulating the Cu oxidation state has been shown to be another strategy, whereas the Cu<sup>(I)</sup> oxidation state cannot be well maintained during electroreduction process. Ingeniously, as displayed in Fig. 5e, electrolyte engineering enables continuous regulation of the reaction system, allowing comprehensive optimization of the reaction conditions. Some oxidizing additives can continuously react with the original catalysts, facilitating the generation and maintenance of high oxidation states in the catalysts. This ensures that the active sites remain in their optimal states during the reaction process, promoting the adsorption of intermediates and enhancing the reaction efficiency. Accordingly, selecting an appropriate additive to stabilize the valence state of Cu<sup>(I)</sup> can effectively promote acidic CO<sub>2</sub>RR toward C<sub>2+</sub> products. Our group proposed an iodine (I<sub>2</sub>)-added strategy, in which the Cu oxidation states were dynamically controlled and a dynamic Cu<sup>0</sup>/Cu<sup>+</sup> surface was constructed, enabling efficient acidic CO<sub>2</sub>RR in a low-concentration cation electrolyte.<sup>75</sup> The ATR-FTIR and density functional theory (DFT) calculation results revealed that this unique Cu<sup>0</sup>/Cu<sup>+</sup> interface reinforced the adsorption of the \*CO intermediate on Cu catalysts, promoting the C-C coupling process. Consequently, a high SPCE of 54% at 2.5 sccm and a C<sub>2+</sub> FE of 70% at a current density range of 0.4–0.6 A cm<sup>-2</sup> were achieved in an acidic electrolyte (pH = 1.2) containing 0.3 M K<sup>+</sup> and 20 mM I<sub>2</sub>, outperforming its counterparts without the addition of I<sub>2</sub> (Fig. 5f).

## 5.2 Catalyst modification

Following the resolution and investigation of electrolyte issues, designing electrocatalysts to further promote the performance

of acidic CO<sub>2</sub>RR has become a prominent focus. Research has revealed that an ideal electrocatalyst for CO<sub>2</sub>RR should possess moderate adsorption capability for the CO<sub>2</sub>RR intermediates, while maintaining a lower \*H adsorption ability to favour CO<sub>2</sub>RR over HER.<sup>58</sup> Thus, rationally modulating the electronic and geometric structures of catalysts is conducive to the mass and electronic transport during acidic CO<sub>2</sub>RR. Similar to alkaline systems, catalyst modification strategies also involve morphology optimization, atomic-scale regulation, and material phase engineering in acidic CO<sub>2</sub>RR. A summary of the detailed acidic CO<sub>2</sub>RR performances driven by catalyst modification is presented in Table 2, and the corresponding elaboration is discussed below.

**5.2.1 Morphology optimization.** The optimization of the morphology of catalysts to control their porosity, particle size, and active site distribution and enhance the mass transport has already been applied in various electrocatalytic reactions. In acidic CO<sub>2</sub>RR, some studies designed various catalyst morphologies to trap K<sup>+</sup> and OH<sup>-</sup>, thereby creating a CO<sub>2</sub>RR-favorable local environment (Fig. 6a).<sup>61,105,106,123</sup> For example, to modulate the catalyst-electrolyte interface microenvironment, Ma *et al.* synthesized Cu porous nanosheets (ER-CuNS) *via* the hydrothermal and electroreduction method.<sup>23</sup> CO<sub>2</sub>RR-favorable species, such as K<sup>+</sup> and OH<sup>-</sup>, accumulated on the Helmholtz plane, decreased the surface binding of protons and facilitated C-C coupling. Thereby, an excellent C<sub>2+</sub> FE of 83.7% and SPCE of 54.4% were achieved in 0.05 M H<sub>2</sub>SO<sub>4</sub> with 3.0 M KCl (pH ≤ 1). Porous carbon-coated Fe nanoparticles (FeNPs-NC) were synthesized through ion adsorption and pyrolysis with zeolitic imidazolate framework-8 (ZIF-8) as the precursor and utilized as catalysts for acidic CO<sub>2</sub>RR conversion to CO.<sup>100</sup> By controlling the amount of Fe<sup>3+</sup>, the size of the Fe particles was adjusted. The results showed that FeNPs-NC-200 presented the best CO<sub>2</sub>RR performance of above 90% FE<sub>CO</sub> at -0.6 V<sub>RHE</sub>, while FE<sub>CO</sub> decreased with an increase in the Fe ratio owing to the gradual loss of the carbon sheath. ATR-FTIR measurements demonstrated that the porous carbon shell altered the chemical microenvironment, creating a CO<sub>2</sub>-rich environment that boosted the CO<sub>2</sub>RR to CO production under low-pH conditions. In a similar approach, Chi *et al.* engineered vertically grown Bi nanosheets to form cavities that acted as electrolyte reservoirs, preventing OH<sup>-</sup> out-diffusion and H<sup>+</sup> in-diffusion.<sup>101</sup> As a result, a formic acid FE of 96.3% could be achieved with a partial current density of 471 mA cm<sup>-2</sup> at pH 2, together with a full-cell formic acid EE of 40% and SPCE of 79%. Utilizing SiO<sub>2</sub> as the template and resorcinol-formaldehyde as the carbon source, Ag nanoparticles were deposited on the inner surface of hollow carbon spheres (Ag@C) through Stöber coating and chemical etching methods.<sup>102</sup> The confinement of the local alkaline environment significantly enhanced the CO<sub>2</sub>RR process, reaching a CO FE of 95% in an acidic electrolyte with a pH of 1.1 and an SPCE of 46.2% at 2 sccm. Similarly, taking advantage of the limiting proton diffusion effect of the yolk-shell structure, Ni nanoparticles coated in cavities of N-doped carbon nanocages (Ni<sub>5</sub>@NCN) displayed a good acidic CO<sub>2</sub>RR performance of 84.3% FE<sub>CO</sub> at pH 2.5.<sup>103</sup> Further, finite

Table 2 Acidic CO<sub>2</sub>RR performance driven by catalyst modification

Category	Catalyst	Electrolyte	Main products	FE	SPCE	Stability Ref.
Morphology optimization	Electro-reduced porous Cu nanosheets	0.05 M H <sub>2</sub> SO <sub>4</sub> + 3 M KCl (pH < 1)	C <sub>2+</sub>	83% (670 mA cm <sup>-2</sup> )	54.4% (2 sccm)	30 h 23
	Porous carbon-coated Fe nanoparticles	0.2 M H <sub>2</sub> SO <sub>4</sub> + 0.1 M KCl (pH = 3.4)	CO	90% (−0.6 V <sub>RHE</sub> )	—	— 100
	Vertically grown Bi nanosheets	0.05 M H <sub>2</sub> SO <sub>4</sub> + 0.5 M K <sub>2</sub> SO <sub>4</sub> (pH = 2)	HCOOH	96.3% (489 mA cm <sup>-2</sup> )	79% (1 sccm)	45 h 101
	Hollow-structured Ag@C	0.5 M K <sub>2</sub> SO <sub>4</sub> (pH = 1.1)	CO	95% (300 mA cm <sup>-2</sup> )	46.2% (2 sccm)	9 h 102
	N-doped carbon nanocages	0.25 M Na <sub>2</sub> SO <sub>4</sub> + 1 mM H <sub>2</sub> SO <sub>4</sub> (pH = 2.5)	CO	84.3% (−0.6 V <sub>AgCl/Ag</sub> )	—	15 h 103
	N-high-curvature Cu nanoneedle catalyst	3 M KCl + HCl (pH = 1)	C <sub>2+</sub>	90.69% (1400 mA cm <sup>-2</sup> )	25.49% (7 sccm)	8 h 61
	Cu hollow fibre penetration electrode	H <sub>2</sub> SO <sub>4</sub> + 3 M KCl (pH = 0.71)	C <sub>2+</sub>	73.4% (3000 mA cm <sup>-2</sup> )	51.8% (2 sccm)	100 h 104
Ag penetration electrodes	Ag penetration electrodes	0.05 M H <sub>2</sub> SO <sub>4</sub> + 3 M KCl (pH = 1) 1 M Na <sub>2</sub> SO <sub>4</sub> + H <sub>2</sub> SO <sub>4</sub> (pH = 2.7)	CO	95% (4300 mA cm <sup>-2</sup> )	85% (5 sccm)	200 h 105
	3D porous electrode with Bi/C nanoparticles	HCOOH	89.2% (−0.6 V <sub>full cell</sub> )	—	—	24 h 106
Atomic-scale regulation	Ni-N-C catalyst	H <sub>2</sub> SO <sub>4</sub> + 0.5 M K <sub>2</sub> SO <sub>4</sub> (pH = 0.5) 0.5 M H <sub>3</sub> PO <sub>4</sub> + 0.5 M KH <sub>2</sub> PO <sub>4</sub> + 1.5 M KCl (pH CO = 2)	CO	95% (500 mA cm <sup>-2</sup> )	—	8 h 76
	Ni SAs	0.005 M H <sub>2</sub> SO <sub>4</sub> + 3 M KCl (pH = 1.67) H <sub>2</sub> SO <sub>4</sub> + 0.5 M K <sub>2</sub> SO <sub>4</sub> (pH = 2) H <sub>2</sub> SO <sub>4</sub> + 0.5 M K <sub>2</sub> SO <sub>4</sub> (pH = 2)	HCOOH	100% (260 mA cm <sup>-2</sup> )	95%	15 h 55
	NU-1000-Sn with ditin sites	0.05 M H <sub>2</sub> SO <sub>4</sub> + 3 M KCl (pH = 1)	C <sub>2+</sub>	42.2% (320 mA cm <sup>-2</sup> )	—	— 108
	Cu-based cluster compound (Inz-Cu <sub>3</sub> )	H <sub>2</sub> SO <sub>4</sub> + 3 M KCl (pH = 1)	C <sub>2+</sub>	89% (500 mA cm <sup>-2</sup> )	68% (2 sccm)	4.5 h 42
	Pd-Cu catalyst	H <sub>2</sub> SO <sub>4</sub> + 3 M KCl (pH = 1)	C <sub>2+</sub>	86.2% (900 mA cm <sup>-2</sup> )	74.5% (3 sccm)	40 h 109
	La-doped Cu hollow sphere	H <sub>2</sub> SO <sub>4</sub> + 3 M KCl (pH = 1)	HCOOH	91% (1200 mA cm <sup>-2</sup> )	77.4% (3 sccm)	130 h 110
Phase engineering	Cu <sub>6</sub> Sn <sub>5</sub> catalysts	0.05 M H <sub>2</sub> SO <sub>4</sub> + 3 M KCl (pH = 1) 0.05 M H <sub>2</sub> SO <sub>4</sub> + 3 M KCl (pH = 1)	C <sub>2+</sub>	56.5% (−1.9 V <sub>RHE</sub> )	49.3% (1.5 sccm, C <sub>2+</sub> ) (oxygenates)	130 h 111
	High-roughness Ag-Cu alloy catalyst	H <sub>2</sub> SO <sub>4</sub> + 3 M KCl (pH = 4) 0.005 M H <sub>2</sub> SO <sub>4</sub> + 0.5 M K <sub>2</sub> SO <sub>4</sub> (pH = 2) 0.05 M H <sub>2</sub> SO <sub>4</sub> + 0.5 M K <sub>2</sub> SO <sub>4</sub> (pH = 2) H <sub>2</sub> SO <sub>4</sub> + 0.5 M K <sub>2</sub> SO <sub>4</sub> (pH = 3)	C <sub>2+</sub>	70% (400 mA cm <sup>-2</sup> ) 81.8% (410 mA cm <sup>-2</sup> ) 82.4% (400 mA cm <sup>-2</sup> ) 92.15% (200 mA cm <sup>-2</sup> )	31% (12 sccm, C <sub>2+</sub> ) 60% (1 sccm, C <sub>2+</sub> ) — 36.43% (5 sccm)	150 h 112 80 h 113 24 h 114 14 h 62
Specialized types of catalysts	Cobalt protoporphyrin immobilized on a pyrolytic graphite electrode	0.1 M perchlorate solution saturated with CO <sub>2</sub> (pH = 3)	CO	60% (−0.6 V <sub>RHE</sub> )	—	— 66
	CoPe@HCl/Cu-PFSA	0.5 M H <sub>3</sub> PO <sub>4</sub> + 0.5 M KH <sub>2</sub> PO <sub>4</sub> + 2.5 M KCl	C <sub>2+</sub>	82% (800 mA cm <sup>-2</sup> )	90% (2 sccm)	16 h 115
	Nickel phthalocyanine electrocatalysts on carbon nanotubes	H <sub>2</sub> SO <sub>4</sub> + 0.5 M K <sub>2</sub> SO <sub>4</sub> (pH = 2)	CO	98% (400 mA cm <sup>-2</sup> )	—	12 h 116
	EDTA/CuPc/CNP	0.005 M H <sub>2</sub> SO <sub>4</sub> (pH = 2)	CH <sub>4</sub>	71% (100 mA cm <sup>-2</sup> )	78% (0.1 sccm)	300 min 117
	CoTAApC@CNT	0.05 M H <sub>2</sub> SO <sub>4</sub> + 3 M KCl (pH = 1)	CO	93.3% (609.7 mA cm <sup>-2</sup> )	84% (1 sccm)	8 h 118
	CoPe@CNT catalyst	H <sub>2</sub> SO <sub>4</sub> (pH = 1)	CO	60% (30 mA cm <sup>-2</sup> )	—	13 h 60
	Imidazole-linked COF (PcNi-im)	0.01 M H <sub>2</sub> SO <sub>4</sub> + 3 M KCl (pH = 1)	CO	100% (320 mA cm <sup>-2</sup> )	—	10 h 119
	CoPe-CTF	0.5 M H <sub>3</sub> PO <sub>4</sub> + 0.5 M KH <sub>2</sub> PO <sub>4</sub> + 1.5 M KCl (pH CO = 2)	CO	94.3% (−1.5 V <sub>RHE</sub> )	—	10 h 120
	NiPc-NiTAA	0.5 M K <sub>2</sub> SO <sub>4</sub> + H <sub>2</sub> SO <sub>4</sub> (pH = 2)	CO	95.1% (−1.5 V <sub>RHE</sub> )	—	6 h 121
	Cs <sub>3</sub> Bi <sub>2</sub> Br <sub>9</sub> /C	3 mM HBr + 0.5 M CsBr (pH = 2.5)	HCOOH	>80% (−0.75 to −1.25 V <sub>RHE</sub> )	47.2% (2 sccm)	20 h 122

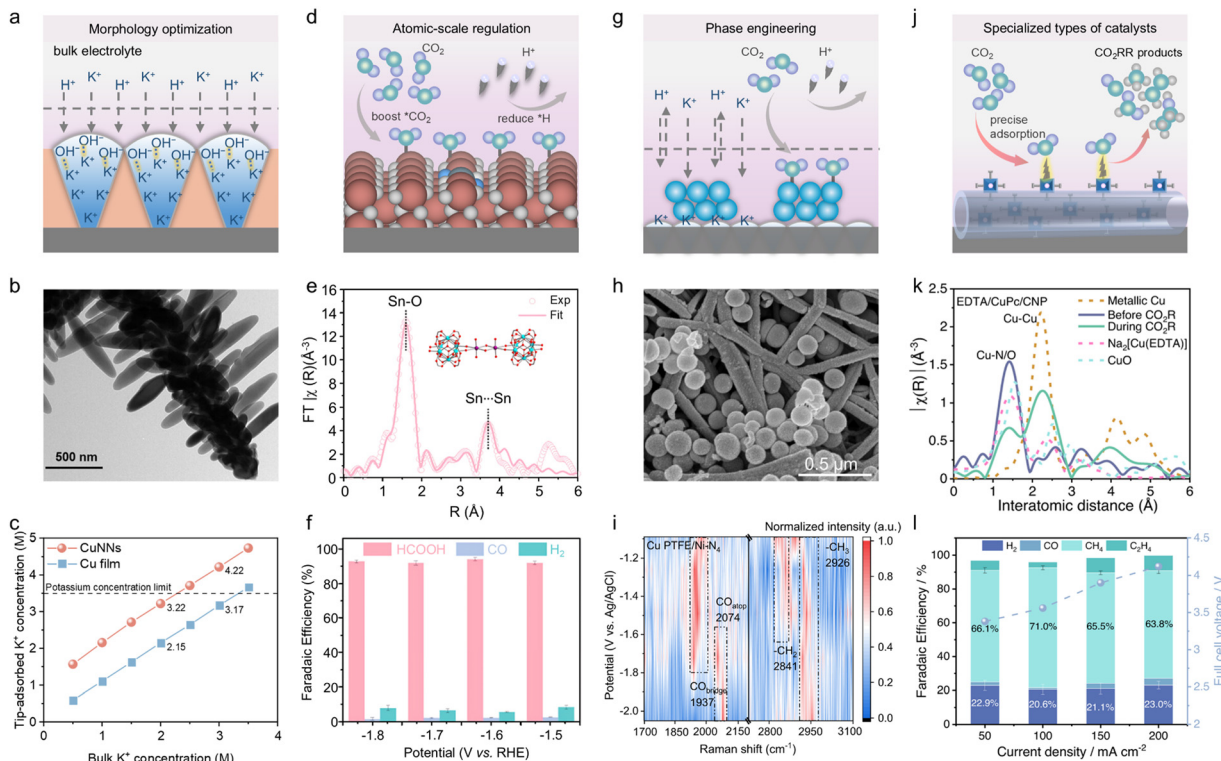


**Fig. 6** (a) Illustration of morphology optimization for trapping  $\text{K}^+$  and  $\text{OH}^-$ . (b) and (c) Needle structure of CuNNs shown using TEM and comparison of surface-adsorbed  $\text{K}^+$  concentration between CuNNs and the Cu film.<sup>61</sup> Reproduced with permission from ref. 61. Copyright 2023, Wiley-VCH. (d) Illustration of atomic-scale regulation on catalysts for promoting acidic  $\text{CO}_2$ RRs. (e) and (f) EXAFS fitting curve, confirming the existence of the ditin sites and corresponding performance.<sup>55</sup> Reproduced with permission from ref. 55. Copyright 2023, the American Chemical Society. (g) Illustration of phase engineering on catalysts to synergistically promote acidic  $\text{CO}_2$ RRs. (h) and (i) SEM image of Cu PTFE/Ni-N<sub>4</sub> composite and *in situ* Raman results of Cu PTFE/Ni-N<sub>4</sub> in an acidic  $\text{CO}_2$ RR.<sup>114</sup> (j) Illustration of precise modulation of specialized catalysts to promote  $\text{CO}_2$ RR intermediate adsorption. (k) and (l) *In situ* extended X-ray absorption fine structure spectra of EDTA/CuPc/CNP before and during the  $\text{CO}_2$ RR, showing the multidentate chelation constraining effect for preventing Cu agglomeration and the existence of Cu-N/O single sites, and corresponding performance.<sup>117</sup>

element simulations using COMSOL demonstrated that nano-needle structures with high curvature can reinforce the  $\text{K}^+$  accumulation on the cathode surface due to the strong local electronic field.<sup>61,101</sup> A high-curvature Cu nanoneedle catalyst (Cu NNs) was found to surpass the KCl dissolution limit (3.5 M) in the bulk electrolyte, enabling the local concentration of  $\text{K}^+$  to reach an impressive 4.22 M (Fig. 6b and c).<sup>61</sup> In the *in situ* ATR-FTIR analysis revealed that this ultra-high local concentration of  $\text{K}^+$  favoured the generation of the \*CO intermediate and promoted the further \*CO dimerization process. Thereby, a  $\text{C}_{2+}$  FE of over 90.69% could be achieved at  $1400 \text{ mA cm}^{-2}$  in the acidic electrolyte with a pH value of 1, together with a 25.49% SPCE at 7 sccm. Employing the penetration configuration for  $\text{CO}_2$  coverage, a Cu hollow fibre penetration electrode (Cu HPE) was fabricated through a phase-inversion and sintering process, facilitating the \*CO adsorption and C-C coupling process and yielding an FE of 73.4% and SPCE of 51.8% for  $\text{C}_{2+}$  products with 100 h stability in the electrolyte with a pH of 0.71.<sup>104</sup> Based on the same design concept, Ag penetration electrodes presented a CO FE of 95% at  $4.3 \text{ A cm}^{-2}$  in a solution with a pH of 1, coupled with 200 h stability and an SPCE of 85%.<sup>105</sup> Different from the widely used GDE, Yan *et al.* developed a 3D porous electrode featuring interconnected channels,

high porosity, and optimized wettability, contributing to a high local pH and enhanced mass transport.<sup>106</sup> With Bi/C nanoparticles as the active component, the FE for formic acid approached 89.2% in a flow cell at pH 2.7. These studies illustrate that morphology modification effectively induces the surface confinement effect, regulating the mass transport at the catalyst-electrolyte interface, and achieving outstanding acidic  $\text{CO}_2$ RR performances.

**5.2.2 Atomic-scale regulation.** Atomic-scale regulation of catalysts, including single atoms (SAs), dual atoms (DAs) and heteroatom doping, has been advanced in the field of acidic  $\text{CO}_2$ RR to optimize the electronic and coordination environments of catalysts, promoting the interfacial adsorption of \* $\text{CO}_2$ -related intermediates and further the  $\text{CO}_2$ RR performance (Fig. 6d).<sup>124,125</sup> Ni SAs dispersed on a porous amorphous carbon framework (Ni-N-C) showed a CO FE of 95% at  $500 \text{ mA cm}^{-2}$  coupled with an outstanding EE of 45% at pH 0.5.<sup>76</sup> Additionally, the  $\text{CO}_2$  loss decreased by 86% at  $300 \text{ mA cm}^{-2}$  in contrast to alkaline conditions. Employing carbon black, porphyrin, and nickel salts, Ni atoms dispersed on carbon were synthesized by Wu *et al.*, exhibiting a high CO FE of 99.9% at the current density of  $300 \text{ mA cm}^{-2}$  under acidic conditions (pH = 2).<sup>107</sup> Moreover, bimetallic-site dual-atom DA

catalysts offer additional active sites and enable fine-tuning of the electronic structure of the active sites by regulating the types and spacing of atomic metals. Xue *et al.* developed an innovative ditin-site electrocatalyst, named NU-1000-Sn, *via* the “ship-in-a-bottle” strategy.<sup>55</sup> *Operando* ATR-FTIR spectroscopy demonstrated that the ditin( $\text{v}$ ) sites, fixed in the nanopores of a metal-organic framework and spaced 3.72 Å apart, were beneficial for the conversion of  $\text{CO}_2$  into the formic acid-related intermediate  $\text{HCOO}^*$ .

Thus, this bridging ditin structure displayed exceptional activity, delivering almost 100% FE for formic acid at 260 mA  $\text{cm}^{-2}$  in an acidic electrolyte (pH = 1.67) with a high SPCE of 95% (Fig. 6e and f). By further increasing the number of atoms, clusters were formed. Wang *et al.* designed a stable, cyclically symmetrical Cu-based cluster compound ( $\text{Inz-Cu}_3$ ) by linking the indazole ligand with Cu salts. The asymmetric Cu active sites in  $\text{Inz-Cu}_3$  helped stabilize the  $\text{C}_2\text{H}_5\text{OH}$ -related intermediate  $^*\text{CHOHCH}_3$ , leading to a  $\text{C}_{2+}$  selectivity of 42.2% in an acidic electrolyte.<sup>108</sup> Furthermore, heteroatom doping can trigger the redistribution of charge and adjustment of intermediate adsorption energy. To balance the  $^*\text{H}$  and  $^*\text{CO}$  coverage on the cathode surface, Xie *et al.* explored the incorporation of various metals with different  $^*\text{CO}$  affinity into Cu catalysts to reduce the  $^*\text{H}$  binding.<sup>42</sup> After screening based on DFT calculations of the Gibbs free energies for the formation of  $\text{CHO}^*$  ( $\text{C}_1$  pathway) and  $\text{OCCOH}^*$  ( $\text{C}_2$  pathway) on the 111 facets, Pd–Cu emerged as the most promising candidate for  $\text{C}_{2+}$  production in acidic  $\text{CO}_2\text{RR}$ . Using the optimally designed Pd–Cu catalyst, a crossover-free system was realized, yielding a  $\text{C}_{2+}$  FE of 89% at 500 mA  $\text{cm}^{-2}$  and a  $\text{C}_{2+}$  SPCE of 60%. Combining the microenvironment regulation through morphology optimization with intrinsic activity enhancement *via* heteroatom doping, an La-doped Cu channel-filled hollow sphere was synthesized using the solvothermal method, followed by electrochemical reduction.<sup>109</sup> The Fourier-transformed extended X-ray absorption fine structure spectrum (FT-EXAFS) results revealed that La on the Cu surface existed as  $\text{La-O}_x$ . The resulting La–O–Cu sites facilitated the adsorption of  $^*\text{CO}$  and the further C–C coupling process, and simultaneously the channel-filled structure drove the accumulation of  $\text{K}^+$  at the cathode, constructing an alkaline local environment, which suppressed HER. Consequently, a  $\text{C}_{2+}$  product FE of 86.2% and a  $\text{C}_{2+}$  SPCE of 52.8% were achieved at the current density of 900 mA  $\text{cm}^{-2}$ .

**5.2.3 Phase engineering.** Phase engineering, which involves adjusting material phases and crystalline structures, is a widely utilized strategy to fine-tune electronic structures, optimize the active sites, and promote mass transport in electrocatalysis. Moreover, the presence of multiple phases within catalysts can induce synergistic effects to drive a high-cation interface and adsorb the  $\text{CO}_2\text{RR}$ -related intermediates effectively (Fig. 6g). In the development of acidic  $\text{CO}_2\text{RR}$ , Yu *et al.* adopted alloying engineering to introduce the oxygen-affinity p-block metal Sn into Cu to shift the product selectivity from CO to formic acid.<sup>110</sup> By performing Gibbs free energy calculations on different intermediates across a series of Cu–Sn alloy models under experimental conditions, it was found that

$\text{Cu}_6\text{Sn}_5$  catalysts exhibited strong  $^*\text{OCHO}$  affinity and weak  $^*\text{H}$ , making them more suitable for  $\text{CO}_2$ -to-formic acid conversion than the pure Cu or Sn. As a result, the  $\text{Cu}_6\text{Sn}_5$  catalysts achieved a 91% FE for formic acid at 1.2 A  $\text{cm}^{-2}$  in a pH 1 acidic electrolyte, with an SPCE of 77.4% at 0.5 A  $\text{cm}^{-2}$ . A high-roughness Ag–Cu alloy catalyst (r-CuAg) synthesized by electrochemical reduction was employed for acidic  $\text{CO}_2\text{RR}$  to increase the production of  $\text{C}_{2+}$  oxygenates (ethanol, *n*-propanol and acetate).<sup>111</sup> The results showed that while the total  $\text{C}_{2+}$  FEs were nearly similar, the rough Cu catalyst predominantly produced  $\text{C}_2\text{H}_4$ , whereas the introduction of Ag shifted the product distribution towards  $\text{C}_{2+}$  oxygenates. According to the *in situ* Raman and DFT calculation results, the high surface roughness combined with alloying effects in r-CuAg facilitated the creation of a high local pH and enriched  $^*\text{CO}$  binding, contributing to a significant  $\text{C}_{2+}$  oxygenate FE of 56.5% at  $-1.9$  V<sub>RHE</sub> in strong acid (pH = 0.75). Additionally, due to the neighbouring site effect observed in alloying catalysts, a series of Zn-incorporated Cu alloy catalysts exhibited excellent asymmetric  $^*\text{CO}$  binding and surface coverage properties.<sup>112</sup> These characteristics benefited C–C coupling, resulting in a  $\text{C}_{2+}$  FE of 70% and SPCE of 31% at 400 mA  $\text{cm}^{-2}$  in acid electrolyte with a pH of 4. The material composite-assisted method is also an effective way to promote the acidic  $\text{CO}_2\text{RR}$  performance of typical catalysts in acidic  $\text{CO}_2\text{RR}$ . Wu *et al.* incorporated amine into Cu nanoparticles to regulate the wettability of the catalyst surface and balance the adsorption ratio of  $^*\text{CO}$  and  $^*\text{H}$ .<sup>113</sup> Therefore, the high  $^*\text{CO}$  coverage contributed to the high FE for  $\text{C}_{2+}$  alcohols of 52.6% on *n*-butylamine-modified Cu at 410 mA  $\text{cm}^{-2}$ , together with a  $\text{C}_{2+}$  SPCE of about 60%. A tandem strategy based on spatial decoupling was proposed to deploy multiple distinct catalysts, enabling CO generation and dimerization, respectively. By coating CO-generating Ni SAs on Cu, a tandem catalyst (Cu PTFE/Ni–N<sub>4</sub>) was fabricated by Wang *et al.*, which presented increased linear  $^*\text{CO}_{\text{atop}}$  adsorption compared with pure Cu (Fig. 6h and i).<sup>114</sup> Thus, the  $\text{C}_{2+}$  FE could reach 82.4% at 400 mA  $\text{cm}^{-2}$ ; meanwhile, the tandem catalyst could maintain a  $\text{C}_{2+}$  FE of 46.5% at 200 mA  $\text{cm}^{-2}$  in a simulated flue gas system as well, demonstrating its practical applicability. Additionally, crystalline structure engineering has been employed by our group to compare the  $\text{CO}_2\text{RR}$  performance of  $\pi$ -phase cubic SnS ( $\pi$ -SnS) with the conventional  $\alpha$ -phase orthorhombic SnS ( $\alpha$ -SnS).<sup>62</sup> Due to the high reduction voltages, SnS was reduced to metallic Sn during  $\text{CO}_2\text{RR}$ . However,  $\pi$ -SnS possessed higher Sn–S binding ability than that of  $\alpha$ -SnS, stabilizing the sulphur species in SnS, benefiting the adsorption of the  $^*\text{OCHO}$  intermediate, and weakening the  $^*\text{H}$  coverage. Therefore, a superior formic acid FE of 92.15% at 0.2 A  $\text{cm}^{-2}$  was achieved together with a carbon efficiency of 36.43%.

**5.2.4 Specialized types of catalysts.** Some specialized types of catalysts have also been adapted for acidic  $\text{CO}_2\text{RR}$ . Notably, molecular electrocatalysts, with highly tunable active sites, can achieve excellent  $\text{CO}_2\text{RR}$  selectivity toward specific products by accurately modulating the metal centres and the ligands (Fig. 6j). In the early stages of acidic  $\text{CO}_2\text{RR}$  development, cobalt protoporphyrin immobilized on pyrolytic graphite was

employed to produce CO and investigate the reaction mechanism of acidic CO<sub>2</sub>RR.<sup>66</sup> Also, research showed that modifying [Ni(cyclam)]<sup>2+</sup> with a carboxylic acid can promote its catalytic activity in aqueous electrolytes.<sup>126</sup> Further, research on molecular electrocatalysts for acidic CO<sub>2</sub>RR declined with the stagnated development of acidic CO<sub>2</sub>RR. However, with the renewed interest in acidic CO<sub>2</sub>RR, molecular electrocatalysts have been further explored for acidic CO<sub>2</sub>RR. Jiang *et al.* dispersed nickel phthalocyanine electrocatalysts (NiPc-OMe) on carbon nanotubes (CNTs), achieving a higher CO FE of 98% in the range of 50 to 400 mA cm<sup>-2</sup> and lower HER competition compared to that of both CoPc-OMe and Ni-Sas, even in strongly acidic media (pH ≤ 1).<sup>116</sup> Utilizing an *in situ* multidentate coordinating strategy, molecules with multi-teeth were employed to modify copper phthalocyanine (CuPc) precursors, confining the Cu(II) species and controlling the cluster sizes.<sup>117</sup> CV tests and CO<sub>2</sub>RR performance screening of the various multidentate molecule-coupled CuPc catalysts revealed that ethylenediaminetetraacetic acid (EDTA) presented the strongest Cu ion chelating ability compared to ethylenediamine (ED) and ethylenediamine-*N,N'*-diacetic acid (EDDA). Together with the constraining effect of conductive carbon nanoparticles (CNP), the EDTA/CuPc/CNP catalyst exhibited low-coordinated Cu clusters by Cu-N/O single sites, favouring the stabilization of \*CHO and \*O key intermediates, thereby promoting CH<sub>4</sub> production (Fig. 6k and l). As the first-step catalyst in a tandem system, atomically dispersed cobalt phthalocyanine was employed to convert CO<sub>2</sub> into CO, combined with the CO-to-C<sub>2+</sub> catalyst comprised of a Cu nanocatalyst with a Cu-ionomer interface, achieving a C<sub>2+</sub> FE of 82% at 800 mA cm<sup>-2</sup>.<sup>115</sup> By functionalizing molecular complexes with quaternary ammonium groups, the catalytic activity of the resulting dodecyl ammonium-functionalized cobalt phthalocyanine (CoTAAPc@CNT) was modulated through the adjusted mass distribution near the active sites. The positively charged and hydrophobic alkylammonium groups suppressed the proton migration, enabling a high CO selectivity of 93% in a wide current density range of 56.2 to 609.7 mA cm<sup>-2</sup>.<sup>118</sup> Then, as a breakthrough in pure acidic CO<sub>2</sub>RR, Feng *et al.* reported a CNT-supported cobalt phthalocyanine (CoPc@CNT) catalyst, featuring Co SAs as active sites, strengthening the adsorption of the \*CO<sub>2</sub> intermediate and achieving a high CO FE of 60% in pure acid (pH = 2).<sup>60</sup> Covalent organic frameworks (COFs), known for their extended skeletons and porous structures, have also been utilized as catalysts for acidic CO<sub>2</sub>RR. An imidazole-linked COF (PcNi-im) synthesized by a condensation reaction presented an almost 100% CO FE at 300 mA cm<sup>-2</sup> in a solution with a pH of 1.<sup>119</sup> The detailed mechanistic study demonstrated that the imidazole groups were protonated into imidazole cation in acid, mitigating CO poisoning, stabilizing the crucial \*COOH intermediate, and boosting the CO<sub>2</sub>RR progress. Additionally, a robust conjugated metallophthalocyanine-based covalent triazine framework (CoPc-CTF) was synthesized *via* a pyrolysis-free process, achieving over 94% FE for CO in the full pH range.<sup>120</sup> Besides, Wan *et al.* designed a metal phthalocyanine (Pc)-based (M = Ni, Co) metal-covalent organic framework linked by metal

tetraaza[14]annulene (TAA), referred to as NiPc-NiTAA and NiPc-CoTAA, respectively. Between them, the optimal NiPc-NiTAA yielded a CO FE of 95.1%, which was attributed to the synergistic interaction between the NiPc and NiTAA active sites, promoting \*COOH adsorption at the reaction interface.<sup>121</sup> Metal halide perovskites, typically recognized as optoelectronic devices, have also been applied for acidic CO<sub>2</sub>RR. Wang *et al.* introduced two Bi-based perovskites (Cs<sub>3</sub>Bi<sub>2</sub>Br<sub>9</sub>/C and Cs<sub>2</sub>AgBiBr<sub>6</sub>/C) for CO<sub>2</sub>-to-HCOOH conversion in acidic electrolyte.<sup>122</sup> The results revealed that Cs<sub>3</sub>Bi<sub>2</sub>Br<sub>9</sub>/C with a lower energy barrier for OCHO\* intermediates could produce a higher HCOOH FE of >80% across the reduction potential range of -0.75 to -1.25 V<sub>RHE</sub>.

### 5.3 Interface optimization

Interface optimization focuses on directly tailoring the interaction zone between the catalyst surface and the electrolyte. It can effectively restrict the transport of H<sup>+</sup> from the bulk electrolyte to the cathode, which in turn promotes the accumulation of alkali cations at the catalyst-electrolyte interface, thereby enhancing the acidic CO<sub>2</sub>RR process. The published studies employed three primary approaches to shift the acidic reaction interfaces in favour of CO<sub>2</sub>RR, enhancing the hydrophobicity/\*OH adsorption, increasing the interfacial cations, and immobilizing the linked cation groups for low-cation or cation-free acidic CO<sub>2</sub>RR. The reported works on acidic CO<sub>2</sub>RR driven by optimizing interfaces are concluded in Table 3 and elaborated in detail as follows.

**5.3.1 Enhancing hydrophobicity/\*OH adsorption.** As shown in Fig. 7a, enhancing the interface hydrophobicity is conducive to modulating the solid-liquid-gas interface and the CO<sub>2</sub>/H<sub>2</sub>O ratio at the cathode, reducing the competitive H<sub>2</sub> generation and alleviating the water flooding phenomenon of the electrode. Besides, adsorbing hydroxyl groups on the cathodic surface has a positive impact on increasing the local alkalinity, promoting the acidic CO<sub>2</sub>RR process. A hydrophobic PTFE layer was introduced to tailor the performance of an Ni-N-C catalyst, achieving an almost 100% CO FE at 250 mA cm<sup>-2</sup> and a high SPCE of 75.7% at 200 mA cm<sup>-2</sup> under 20 sccm CO<sub>2</sub> flow, while without PTFE, the FE of CO only reached 90%.<sup>127</sup> Additionally, due to the water-flooding-resistant ability of PTFE, the PTFE-protected Ni-N-C maintained stability for 36 h in an electrolyte with a pH of 2. Similarly, a hydrophobic SiO<sub>2</sub> layer was applied to protect Cu nanoparticles from structural reconstruction during CO<sub>2</sub>RR, modulating the \*CO adsorption behaviour and promoting the C-C coupling process.<sup>128</sup> Thus, the Cu/SiO<sub>2</sub> catalyst achieved a C<sub>2+</sub> product FE of 76.9% at 900 mA cm<sup>-2</sup> in a strongly acidic environment (pH = 1) (Fig. 7b). Sun *et al.* developed an innovative ultrathin Cu-GDE structure with high-density porosity and super-hydrophobicity by incorporating electrooxidation-synthesized needle-like porous Cu with a 1-octadecanethiol water barrier. With this optimal structure, the Cu-GDE could maintain its functionality even after bending and twisting, achieving a high C<sub>2+</sub> product FE of 87% at 1.6 A cm<sup>-2</sup> under acidic conditions. Cao *et al.* synthesized a Cu catalyst with high \*OH coverage through *in situ*

**Table 3** Acidic CO<sub>2</sub>RR performance driven by interface optimization

Category	Catalyst	Electrolyte	Main products	FE	SPCE	Stability Ref.
Enhancing hydrophobicity/*OH adsorption	Ni-N-C/PTFE	1 M Cs <sub>2</sub> SO <sub>4</sub> + H <sub>2</sub> SO <sub>4</sub> (pH = 2)	CO	100% (250 mA cm <sup>-2</sup> )	75.7% (20 sccm) 34.8% (20 sccm)	36 h 127
	Cu/SiO <sub>2</sub>	0.05 M H <sub>2</sub> SO <sub>4</sub> + 3 M KCl (pH = 1)	C <sub>2+</sub>	76.9% (900 mA cm <sup>-2</sup> )	42% (5 sccm) 3.5% (5 sccm)	12.5 h 128
	Cu/1-octadecanethiol GDE	1 M KCl + 1 M HCl (pH = 1)	C <sub>2+</sub>	87% (1600 mA cm <sup>-2</sup> )	—	10 h 44
Electrodeposited Cu catalyst	0.05 M H <sub>2</sub> SO <sub>4</sub> + 2.5 M KCl (pH = 1)	C <sub>2+</sub>	90% (250 mA cm <sup>-2</sup> )	70% (0.5 sccm) 65% (0.5 sccm)	10 h 39	
	SiC-Nafion/SnBi/PTFE	0.05 M H <sub>2</sub> SO <sub>4</sub> + 3 M KCl (pH = 1)	HCOOH	92% (100–800 mA cm <sup>-2</sup> )	65% (3 sccm) —	125 h 20
	SiC-Nafion/Cu/PTFE	0.05 M H <sub>2</sub> SO <sub>4</sub> + 3 M KCl (pH = 1)	C <sub>2+</sub>	65–70% (100–800 mA cm <sup>-2</sup> )	—	35 h 20
	SiC-Nafion/Ag/PTFE	0.05 M H <sub>2</sub> SO <sub>4</sub> + 3 M KCl (pH = 1)	CO	92% (100 mA cm <sup>-2</sup> )	—	52 h 20
	Electrostatic carbon/Cu/PTFE	0.5 M K <sub>2</sub> SO <sub>4</sub> + H <sub>2</sub> SO <sub>4</sub> (pH = 2)	C <sub>2</sub> H <sub>4</sub>	64.5% (300 mA cm <sup>-2</sup> )	—	— 129
Increasing interfacial cations	1 M H <sub>3</sub> PO <sub>4</sub> + 3 M KCl (pH < 1)	C <sub>2+</sub>	50% (1200 mA cm <sup>-2</sup> )	77% (3 sccm) 75% (3 sccm)	12 h 24	
	COF:PFSA-modified PTFE–Cu electrode	1 M H <sub>3</sub> PO <sub>4</sub> + 3 M KCl (pH < 1)	C <sub>2+</sub>	75% (200 mA cm <sup>-2</sup> )	30 h 25	
	CoPc@HC/Cu-PFSA	0.5 M H <sub>3</sub> PO <sub>4</sub> + 0.5 M KH <sub>2</sub> PO <sub>4</sub> + 2.5 M KCl	C <sub>2+</sub>	82% (800 mA cm <sup>-2</sup> )	90% (0.5 sccm) 90% (2 sccm)	16 h 115
Surface iodine and PGDY co-modified Bi catalyst	0.5 M K <sub>2</sub> SO <sub>4</sub> (pH = 3.5)	HCOOH	90% (110 mA cm <sup>-2</sup> )	—	240 h 130	
Phenyldiazonium-modified Cu	1 M H <sub>3</sub> PO <sub>4</sub> /1 M KCl (pH = 1)	C <sub>2+</sub>	65% (100 mA cm <sup>-2</sup> )	—	6 h 43	
18-Crown-6/Cu	0.5 M K <sub>2</sub> SO <sub>4</sub> + H <sub>2</sub> SO <sub>4</sub> (pH = 2)	CH <sub>4</sub>	51.2% (600 mA cm <sup>-2</sup> )	50.4% (2 sccm) 55% (50 mA cm <sup>-2</sup> )	16 000 s 131	
Immobilizing cation group for low-cation or cation-free acidic CO <sub>2</sub> RR	n-Tolyl pyridinium modified-Cu QAPPt and PTFE-modified Ag catalyst	1.0 M H <sub>3</sub> PO <sub>4</sub> + 0.1 M KH <sub>2</sub> PO <sub>4</sub> (pH = 1)	C <sub>2+</sub>	—	5 h 63	
	CuNP-EMIM	0.1 M H <sub>2</sub> SO <sub>4</sub> (pH = 0.7)	All CO <sub>2</sub> RR products	95.6% (100 mA cm <sup>-2</sup> ) 11% (100 mA cm <sup>-2</sup> )	—	400 min 132
Cationic-group-functionalized Cu	0.2 M H <sub>2</sub> SO <sub>4</sub> (pH = 0.4)	C <sub>2+</sub>	80% (100 mA cm <sup>-2</sup> )	90% (0.2 sccm)	150 h 45	
PDDA/GO-modified Ag catalyst	0.01 M H <sub>2</sub> SO <sub>4</sub> (pH ≈ 2)	CO	85% (100 mA cm <sup>-2</sup> )	—	50 h 47	
c-PDDA-modified Ag catalyst	0.1 M H <sub>2</sub> SO <sub>4</sub> (pH = 1)	CO	95% (100 mA cm <sup>-2</sup> )	—	— 48	
c-PDDA-modified indium catalyst	0.1 M H <sub>2</sub> SO <sub>4</sub> (pH = 1)	HCOOH	76% (200 mA cm <sup>-2</sup> )	—	35 h 48	

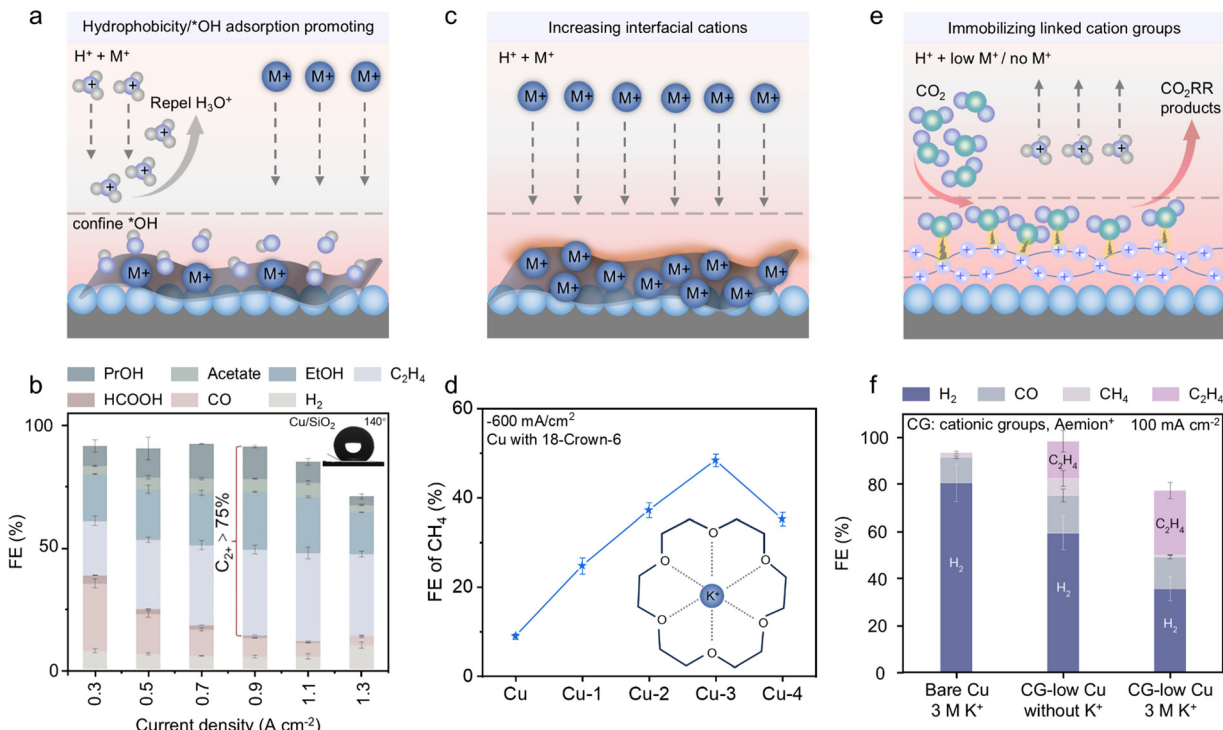


Fig. 7 (a) Illustration of the effect of enhancing hydrophobicity/\*OH adsorption on an acidic CO<sub>2</sub>RR. (b) Product distribution of Cu/SiO<sub>2</sub> at different current densities in an acidic CO<sub>2</sub>RR (inset: the contact angle image of Cu/SiO<sub>2</sub>, showing its hydrophobicity).<sup>128</sup> Reproduced with permission from ref. 128. Copyright 2024, the American Chemical Society. (c) Illustration of promoted cation accumulation on the catalyst interface. (d) CH<sub>4</sub> FE comparison of Cu catalysts with different ratios of 18-crown-6 (inset: the structure of 18-crown-6, showing its ability to coordinate with K $^+$ ).<sup>131</sup> Reproduced with permission from ref. 131. Copyright 2023, Wiley-VCH. (e) Illustration of the effect of immobilizing linked cation groups for a low-cation or cation-free acidic CO<sub>2</sub>RR. (f) Product distribution on bare Cu and CG-low-Cu in acidic electrolytes with/without K $^+$ , showing the influence of CG on acidic CO<sub>2</sub>RR performance.<sup>45</sup> Reproduced with permission from ref. 45. Copyright 2023, Springer Nature.

electrodeposition.<sup>39</sup> *In situ* time-resolved Raman spectroscopy revealed that the  $\text{OH}^*$  species can interact with  $\text{CO}^*$ , thereby enhancing the adsorption of  $\text{CO}^*$  and boosting the C-C coupling process. Further, they introduced amide-bearing polymers during electrodeposition to enhance the selectivity of ethylene, and thereby a high ethylene FE of 60% could be achieved by this optimal electrodeposited Cu catalyst, together with a C<sub>2+</sub> SPCE of 70% and an EE of 30%. Additionally, an electrically nonconductive SiC-Nafion layer was applied to coat CO<sub>2</sub>RR catalysts to regulate the transport of cations and anions, creating an OH $^-$ -rich layer on the cathode during the reaction.<sup>20</sup> The acidic CO<sub>2</sub>RR performance was enhanced towards product selectivity, carbon conversion efficiency and durability among the common metal catalysts, such as SnBi, Ag and Cu. Besides, Wang *et al.* utilized an *in situ* electrostatic confinement strategy to trap OH $^-$  on the Cu/carbon surface.<sup>129</sup> This approach leveraged the negative voltage of CO<sub>2</sub>RR, and the extended electric double layer induced by electrostatic interactions of conductive carbon nanoparticles. *In situ* Raman measurements revealed that the OH $^-$ -rich surface enhanced the formation of Cu-CO and Cu-OH species, promoting C-C coupling and achieving a largely promoted ethylene FE of 64.5% in acidic solution at 300 mA cm $^{-2}$  (pH = 2).

**5.3.2 Increasing interfacial cations.** A high alkali cation distribution at the catalyst-electrolyte interface can strengthen

the electric field, promoting  $\text{CO}^*$  stabilization and improving the CO<sub>2</sub>RR performance. Despite the presence of high concentrations of cations in most bulk electrolytes for acidic CO<sub>2</sub>RR, creating a cation-rich interface during the reaction operation remains challenging. Thus, the implementation of cation-augment layers to forcefully enhance the diffusion of alkali-metal cations towards the catalyst interface is crucial for further improving the selectivity of acidic CO<sub>2</sub>RR (Fig. 7c). In the study by Huang *et al.*, after confirming the positive impact of high-concentration alkali cations on acidic CO<sub>2</sub>RR, a cation-augment layer of perfluorosulfonic acid (PFSA) was introduced.<sup>24</sup> This layer facilitated cation transport from the electrolyte to the catalyst interface; therefore, a K $^+$ -rich interface with high interfacial pH was achieved, facilitating C-C coupling and driving a higher SPCE of 77% and C<sub>2+</sub> FE of 50% at 1.2 A cm $^{-2}$  than its bare Cu counterpart. Furthermore, it has been found that amphoteric covalent organic frameworks (COFs) can help distribute the PFSA ionomer layer uniformly and orientally through electrostatic interactions.<sup>25</sup> Thus, an adlayer comprised of insulating polymer nanoparticles (COF) and PFSA ionomer was constructed, featuring proton confinement and a K $^+$ -rich interface on Cu catalysts, favouring CO<sub>2</sub> activation and achieving a C<sub>2+</sub> FE of 75% at 200 mA cm $^{-2}$ . Taking advantage of the spatially decoupling characteristics of tandem catalysts, Chen *et al.* developed a hollow carbon-supported CoPc

(CoPc@HC) catalyst coupled with Cu layers for continuous  $\text{CO}_2$ -to-CO and CO-to- $\text{C}_{2+}$  conversion.<sup>115</sup> To further enhance the mass transport of CO, a 3D Cu-PFSA interface was introduced, which effectively enhanced the FE of  $\text{C}_2\text{H}_4$  in the acidic electrolyte. Moreover, after modification with iodine and pyrenyl-graphdiyne (PGDY), the  $\text{Bi}_2\text{O}_2\text{CO}_3$  catalyst demonstrated a high FE of over 90% for formic acid production from  $-1.2$  to  $-1.5$  V<sub>RHE</sub>.<sup>130</sup> The detailed analyses illustrated that the surface iodine promoted the adsorption of the \*OCHO intermediate and increased the  $\text{K}^+$  interfacial concentrations; meanwhile, the PGDY layer improved the  $\text{CO}_2$  adsorption and prevented catalyst deactivation. To restrict proton diffusion, phenyldiazonium was applied to the Cu catalyst surface (PD-Cu) through electrodeposition, boosting the selectivity and activity of  $\text{CO}_2$ -to- $\text{C}_{2+}$  conversion.<sup>43</sup> Additionally, 18-crown-6, which can coordinate with  $\text{K}^+$ , was used as an additive on a Cu electrode to enrich interfacial  $\text{K}^+$  concentrations and stabilize \*CO adsorption.<sup>131</sup> The kinetic isotope effect results demonstrated that 18-crown-6 accelerated  $\text{H}_2\text{O}$  dissociation and boosted \*CO hydrogenation, thereby leading to an FE of 51.2% for  $\text{CO}_2$ -to- $\text{CH}_4$  conversion in acid (pH = 2) when the ratio of Cu and 18-crown-6 was 3 (named Cu-3) (Fig. 7d).

**5.3.3 Immobilizing linked cation groups for low-cation or cation-free acidic  $\text{CO}_2\text{RR}$ .** As previously mentioned, the development of acidic  $\text{CO}_2\text{RR}$  has witnessed significant advances through the utilization of high concentrations of alkali cations. However, it has been reported that high-concentration-cation systems are prone to carbonate precipitation during the reaction due to the high local pH and low solubility of carbonate, which can block the gas transport channels and cause water flooding of GDE.<sup>38,45</sup> Consequently, some researchers have shifted their focus to acidic  $\text{CO}_2\text{RR}$  in electrolyte with low-concentration cations or even in pure acid. The primary approach involves immobilizing a long-chain cation group on the catalyst interface to replace the effect of alkali metal cations, constructing a favourable microenvironment to adsorb the  $\text{CO}_2\text{RR}$ -related intermediate effectively (Fig. 7e). Nie *et al.* electrodeposited an *N*-tolyl pyridinium (tolyl-pyr) additive on Cu catalysts, achieving a high  $\text{CO}_2$  conversion efficiency in a low potassium concentration (0.1 M) acidic electrolyte (pH = 2).<sup>63</sup> The RDE-CV tests demonstrated that the organic film weakened the proton transport and attenuated the HER competition during the acidic  $\text{CO}_2\text{RR}$  process. Additionally, a hydrophobic cationic ionomer, quaternary ammonium poly(*N*-methyl-piperidine-*co*-*p*-terphenyl) (QAPPT), and PTFE were adopted as an enhanced layer on Ag catalysts to promote CO production in an MEA electrolyser. A high CO FE of 95.6% was achieved at 100 mA cm<sup>-2</sup> in acidic medium with a low alkali ion concentration of 0.2 M.<sup>132</sup> In a significant breakthrough, Cu nanoparticles modified with electrodeposited pyridinium (CuNP-EMIM) exhibited an FE of 11% for  $\text{CO}_2\text{RR}$  products in a 0.1 M H<sub>2</sub>SO<sub>4</sub> solution without KCl, despite their limited performance.<sup>133</sup> It was claimed that the positive charge at the cathode interface mimicked a  $\text{K}^+$  layer, inhibiting the competing HER. However, the underlying mechanism remains unclear. Furthermore, Fan *et al.* utilized benzimidazolium cationic groups (CG) to replace

the effect of alkali cations and immobilized CG on Cu catalysts, achieving a high  $\text{C}_{2+}$  product FE of 80% and SPCE of 70%, together with the stability of 150 h for  $\text{CO}_2\text{RR}$  in pure acid (Fig. 7f).<sup>45</sup> The experimental and computational studies revealed that CG attenuated the proton migration, increasing the local pH and promoting both the carbon and energy efficiency of acidic  $\text{CO}_2\text{RR}$ . Using a similar strategy, positive-charge polyelectrolyte-poly(diallyldimethylammonium) (PDDA) was stabilized on graphene oxide and coated on an Ag catalyst to substitute alkali cations.<sup>47</sup> The PDDA-GO-modified Ag catalysts showed a CO FE of 85% and EE of 35% at 100 mA cm<sup>-2</sup> in 0.01 M H<sub>2</sub>SO<sub>4</sub>. Additionally, Qin *et al.* immobilized cross-linked poly-diallyldimethylammonium chloride (c-PDDA) as a cation layer to modify the surfaces of Ag and In catalysts, respectively.<sup>48</sup> The results showed that the CO FE reached 95% for modified Ag, together with a formic acid FE of 76% on the modified indium catalyst. The mechanism study revealed that the cationic layer functioned similarly to alkali cations in acidic electrolytes, suppressing H<sup>+</sup> transport and promoting the electric field within the Stern layer.

## 6. Conclusions and outlook

To date,  $\text{CO}_2$  electroreduction under alkaline and neutral conditions has rapidly developed; however, the associated problems have also become evident. For example, the formation of carbonates can cause severe  $\text{CO}_2$  crossover into the anolyte in alkaline and neutral media, significantly reducing the carbon utilization efficiency, and thus driving the development of  $\text{CO}_2\text{RR}$  under acidic conditions. Fortunately, leveraging the advancements in alkaline and neutral  $\text{CO}_2\text{RR}$ , related components such as electrodes, electrolyzers, and membranes have been thoroughly researched and optimized. Therefore, it is a great opportunity to advance the development of acidic  $\text{CO}_2\text{RR}$ . In recent years, studies on acidic  $\text{CO}_2\text{RR}$  have mainly focused on the regulation of the catalyst-electrolyte interface, promoting  $\text{CO}_2$  activation and  $\text{CO}_2\text{RR}$ -related intermediate adsorption in acidic media. The developing strategies can be classified into three aspects including electrolyte engineering for affecting the interfacial catalyst environment and electrolyte structures, modification of the electronic and geometric structures of catalysts to favour the adsorption of the  $\text{CO}_2\text{RR}$ -related intermediates, and interface optimization for hindering proton diffusion and inducing cation augmentation. Additionally, there are also some problems and suggestions regarding this research field as follows.

(1) Development of electrolyzers and related accessories. Despite the continuous development of  $\text{CO}_2\text{RR}$  electrolyzers ranging from H-cells and flow cells to MEA, the operability of these devices is still limited, and experimental errors remain significant, which affects the scientific validity of the experiments. Also, the electrolyte flooding phenomenon still easily occurs and disrupts the entire operation of the reaction. Thus, it is still urgent to further develop next-generation  $\text{CO}_2\text{RR}$  electrolyzers and GDE to enhance the scientific validity and accuracy of experimental results.

(2) Low-cation/cation-free electrolytes for acidic CO<sub>2</sub>RR. Alkali cations play a vital role in the performance of acidic CO<sub>2</sub>RR, however, a high concentration of cations causes carbonate crystallization and blocks the gas transport channels. Given these challenges, only a limited number of studies have successfully achieved high CO<sub>2</sub>RR product selectivity in pure acid, primarily by modifying the interface through the immobilization of large cation groups. However, the operation current density is limited to below 300 mA cm<sup>-2</sup> to date. To advance CO<sub>2</sub>RR in pure acid, it is essential to develop new strategies focused on catalyst structure design and microenvironment modification that enable operation at a higher current density.

(3) Seawater electrolysis. Recently, electrolysis in seawater has emerged as practical technology for conserving freshwater resources and decreasing the technique cost. Various electrocatalytic processes, such as HER, OER, and the oxygen reduction reaction, have made significant progress in acidic/alkaline seawater electrolysis.<sup>134</sup> Reports indicate that chloride anions and alkali cations, which are abundant in seawater, positively influence CO<sub>2</sub>RR.<sup>24,97,135</sup> Also, the salt-rich and complex ionic composition of seawater provides a unique electrolyte environment for acidic CO<sub>2</sub>RR, simplifying the electrolyte preparation process. Also, the acidic electrolyte can react with CO<sub>3</sub><sup>2+</sup>/OH<sup>-</sup>-based participation species to reduce the blockage of the active sites by sediment deposition. Therefore, seawater-based acidic CO<sub>2</sub>RR is anticipated to become an important research area in the future development of CO<sub>2</sub>RR research.

(4) Characterization technologies for dynamic observation of the interfacial cation accumulation during acidic CO<sub>2</sub>RR. Cation accumulation has been verified to effectively promote the performance of CO<sub>2</sub>RR in acidic media. However, most existing techniques, such as zero-potential measurement, nuclear magnetic resonance spectroscopy, and inductively coupled plasma optical emission spectroscopy, are limited to *ex situ* observations. Real-time monitoring of the cation accumulation phenomenon remains a significant challenge. Fluorescent probes and differential interference contrast microscopy, using ion-selective probes and local light refraction as indicators, offer promising options for monitoring real-time cation distributions. However, these techniques require the integration of specialized micro-electrochemical flow cells capable of accommodating the probes and optical lenses, posing significant technical challenges. Thus, developing real-time observation technologies for investigating interfacial composition variations during acidic CO<sub>2</sub>RR is crucial for deeper mechanistic understanding and further optimization of this reaction.

(5) C–N coupling and cascade reaction. Some studies focus on the coupling reaction of CO<sub>2</sub>RR and NO<sub>2</sub><sup>-</sup>/NO<sub>3</sub><sup>-</sup>/N<sub>2</sub>/NH<sub>3</sub> reduction to produce compounds such as urea and amide under neutral and alkaline conditions.<sup>136,137</sup> Thus, it is worthwhile to explore the C–N coupling reaction and the possibility for product diversity in acidic media. Additionally, cascading CO<sub>2</sub>RR with other reactions is conducive to

producing long-chain carbon products, such as chlorohydrin, propyl alcohol, ethylene oxide, and ethyl acetate. However, this exploration is still undeveloped in acidic CO<sub>2</sub>RR. Consequently, developing cascade electrocatalytic systems based on acidic CO<sub>2</sub>RR to produce long-chain carbon products presents a meaningful avenue for further research.

## Author contributions

Y. J., Y. Z., and S.-Z. Q. proposed the topic of the review. Y. J., L. H., and C. C. collaboratively designed and corrected the figures. Y. J. drafted the manuscript. Y. Z., and S.-Z. Q. corrected and reviewed the manuscript prior to submission. All authors contributed to discussions of the review.

## Data availability

No primary research results, software or code have been included and no new data were generated or analysed as part of this review.

## Conflicts of interest

There are no conflicts to declare.

## Acknowledgements

The authors gratefully acknowledge the financial support provided by the Australian Research Council through Discovery Project and Linkage Project Programs (FT200100062, DP230102027, DP240102575, CE230100032, LP210301397). Y. J. is supported by the Chinese CSC Scholarship Program.

## References

- 1 K. O. Yoro and M. O. Daramola, *Advances in Carbon Capture*, 2020, 3–28, DOI: [10.1016/B978-0-12-819657-1.00001-3](https://doi.org/10.1016/B978-0-12-819657-1.00001-3).
- 2 P. Singh, D. Yadav and S. Pandian, *Global Climate Change*, 2021, 79–108, DOI: [10.1016/B978-0-12-822928-6.00009-5](https://doi.org/10.1016/B978-0-12-822928-6.00009-5).
- 3 M. Jiang, H. Wang, M. Zhu, X. Luo, Y. He, M. Wang, C. Wu, L. Zhang, X. Li, X. Liao, Z. Jiang and Z. Jin, *Chem. Soc. Rev.*, 2024, **53**, 5149–5189.
- 4 Z. Wang, Y. Zhou, P. Qiu, C. Xia, W. Fang, J. Jin, L. Huang, P. Deng, Y. Su, R. Crespo-Otero, X. Tian, B. You, W. Guo, D. Di Tommaso, Y. Pang, S. Ding and B. Y. Xia, *Adv. Mater.*, 2023, **35**, 2303052.
- 5 W. Gao, S. Liang, R. Wang, Q. Jiang, Y. Zhang, Q. Zheng, B. Xie, C. Y. Toe, X. Zhu, J. Wang, L. Huang, Y. Gao, Z. Wang, C. Jo, Q. Wang, L. Wang, Y. Liu, B. Louis, J. Scott, A. C. Roger, R. Amal, H. He and S. E. Park, *Chem. Soc. Rev.*, 2020, **49**, 8584–8686.
- 6 W. Lai, Y. Qiao, J. Zhang, Z. Lin and H. Huang, *Energy Environ. Sci.*, 2022, **15**, 3603–3629.

7 P. P. Yang and M. R. Gao, *Chem. Soc. Rev.*, 2023, **52**, 4343–4380.

8 X. Tan, C. Yu, Y. Ren, S. Cui, W. Li and J. Qiu, *Energy Environ. Sci.*, 2021, **14**, 765–780.

9 Z. Yao, X. He and R. Lin, *Electrochem. Energy Rev.*, 2024, **7**, 8.

10 M. Zheng, P. Wang, X. Zhi, K. Yang, Y. Jiao, J. Duan, Y. Zheng and S. Z. Qiao, *J. Am. Chem. Soc.*, 2022, **144**, 14936–14944.

11 L. Li, A. Ozden, S. Guo, A. D. A. F. P. Garcí, C. Wang, M. Zhang, J. Zhang, H. Jiang, W. Wang, H. Dong, D. Sinton, E. H. Sargent and M. Zhong, *Nat. Commun.*, 2021, **12**, 5223.

12 X. She, L. Zhai, Y. Wang, P. Xiong, M. M.-J. Li, T.-S. Wu, M. C. Wong, X. Guo, Z. Xu, H. Li, H. Xu, Y. Zhu, S. C. E. Tsang and S. P. Lau, *Nat. Energy*, 2024, **9**, 154–162.

13 F. Huang, X. Chen, H. Sun, Q. Zeng, J. Ma, D. Wei, J. Zhu, Z. Chen, T. Liang, X. Yin, X. Liu, J. Xu and H. He, *Angew. Chem., Int. Ed.*, 2024, **64**, e202415642.

14 Y. J. Ko, C. Lim, J. Jin, M. G. Kim, J. Y. Lee, T. Y. Seong, K. Y. Lee, B. K. Min, J. Y. Choi, T. Noh, G. W. Hwang, W. H. Lee and H. S. Oh, *Nat. Commun.*, 2024, **15**, 3356.

15 W. Li, C. Yu, X. Tan, Y. Ren, Y. Zhang, S. Cui, Y. Yang and J. Qiu, *ACS Catal.*, 2024, **14**, 8050–8061.

16 B. Shao, D. Huang, R. K. Huang, X. L. He, Y. Luo, Y. L. Xiang, L. B. Jiang, M. Dong, S. Li, Z. Zhang and J. Huang, *Angew. Chem., Int. Ed.*, 2024, **63**, e202409270.

17 H. Wu, L. Huang, J. Timoshenko, K. Qi, W. Wang, J. Liu, Y. Zhang, S. Yang, E. Petit, V. Flaud, J. Li, C. Salameh, P. Miele, L. Lajaunie, B. Roldán Cuenya, D. Rao and D. Voiry, *Nat. Energy*, 2024, **9**, 422–433.

18 M. Esmaeilirad, Z. Jiang, A. M. Harzandi, A. Kondori, M. Tamadoni Saray, C. U. Segre, R. Shahbazian-Yassar, A. M. Rappe and M. Asadi, *Nat. Energy*, 2023, **8**, 891–900.

19 K. Qi, Y. Zhang, N. Onofrio, E. Petit, X. Cui, J. Ma, J. Fan, H. Wu, W. Wang, J. Li, J. Liu, Y. Zhang, Y. Wang, G. Jia, J. Wu, L. Lajaunie, C. Salameh and D. Voiry, *Nat. Catal.*, 2023, **6**, 319–331.

20 L. Li, Z. Liu, X. Yu and M. Zhong, *Angew. Chem., Int. Ed.*, 2023, **62**, e202300226.

21 W. Wu, L. Xu, Q. Lu, J. Sun, Z. Xu, C. Song, J. C. Yu and Y. Wang, *Adv. Mater.*, 2024, **37**, 2312894.

22 T. Zhang, J. Zhou, T. Luo, J. Q. Lu, Z. Li, X. Weng and F. Yang, *Chem. – Eur. J.*, 2023, **29**, e202301455.

23 Z. Ma, Z. Yang, W. Lai, Q. Wang, Y. Qiao, H. Tao, C. Lian, M. Liu, C. Ma, A. Pan and H. Huang, *Nat. Commun.*, 2022, **13**, 7596.

24 J. E. Huang, F. Li, A. Ozden, A. Sedighian Rasouli, F. P. Garcia de Arquer, S. Liu, S. Zhang, M. Luo, X. Wang, Y. Lum, Y. Xu, K. Bertens, R. K. Miao, C. T. Dinh, D. Sinton and E. H. Sargent, *Science*, 2021, **372**, 1074–1078.

25 Y. Zhao, L. Hao, A. Ozden, S. Liu, R. K. Miao, P. Ou, T. Alkayyali, S. Zhang, J. Ning, Y. Liang, Y. Xu, M. Fan, Y. Chen, J. E. Huang, K. Xie, J. Zhang, C. P. O'Brien, F. Li, E. H. Sargent and D. Sinton, *Nat. Synth.*, 2023, **2**, 403–412.

26 H. Yano, F. Shirai, M. Nakayama and K. Ogura, *J. Electroanal. Chem.*, 2002, **519**, 93–100.

27 K. Ogura, H. Yano and F. Shirai, *J. Electrochem. Soc.*, 2003, **150**, D163–D168.

28 H. Yano, T. Tanaka, M. Nakayama and K. Ogura, *J. Electroanal. Chem.*, 2004, **565**, 287–293.

29 T. Lee, Y. Lee, J. Eo and D. H. Nam, *Nanoscale*, 2024, **16**, 2235–2249.

30 X. Cao, D. Tan, B. Wulan, K. S. Hui, K. N. Hui and J. Zhang, *Small Methods*, 2021, **5**, 2100700.

31 J. Li and J. Gong, *Energy Environ. Sci.*, 2020, **13**, 3748–3779.

32 J. Wang, H. Y. Tan, M. Y. Qi, J. Y. Li, Z. R. Tang, N. T. Suen, Y. J. Xu and H. M. Chen, *Chem. Soc. Rev.*, 2023, **52**, 5013–5050.

33 S. Banerjee, Z.-Q. Zhang, A. S. Hall and V. S. Thoi, *ACS Catal.*, 2020, **10**, 9907–9914.

34 H. Khani, A. R. Puente Santiago and T. He, *Angew. Chem., Int. Ed.*, 2023, **62**, e202306103.

35 F. P. Garcia de Arquer, C. T. Dinh, A. Ozden, J. Wicks, C. McCallum, A. R. Kirmani, D. H. Nam, C. Gabardo, A. Seifitokaldani, X. Wang, Y. C. Li, F. Li, J. Edwards, L. J. Richter, S. J. Thorpe, D. Sinton and E. H. Sargent, *Science*, 2020, **367**, 661–666.

36 M. C. O. Monteiro, F. Dattila, B. Hagedoorn, R. García-Muelas, N. López and M. T. M. Koper, *Nat. Catal.*, 2021, **4**, 654–662.

37 J. Gu, S. Liu, W. Ni, W. Ren, S. Haussener and X. Hu, *Nat. Catal.*, 2022, **5**, 268–276.

38 H.-G. Qin, F.-Z. Li, Y.-F. Du, L.-F. Yang, H. Wang, Y.-Y. Bai, M. Lin and J. Gu, *ACS Catal.*, 2023, **13**, 916–926.

39 Y. Cao, Z. Chen, P. Li, A. Ozden, P. Ou, W. Ni, J. Abed, E. Shirzadi, J. Zhang, D. Sinton, J. Ge and E. H. Sargent, *Nat. Commun.*, 2023, **14**, 2387.

40 X. Zhu, J. Huang and M. Eickerling, *Acc. Chem. Res.*, 2024, **57**, 2080–2092.

41 C. P. O'Brien, R. K. Miao, S. Liu, Y. Xu, G. Lee, A. Robb, J. E. Huang, K. Xie, K. Bertens, C. M. Gabardo, J. P. Edwards, C.-T. Dinh, E. H. Sargent and D. Sinton, *ACS Energy Lett.*, 2021, **6**, 2952–2959.

42 Y. Xie, P. Ou, X. Wang, Z. Xu, Y. C. Li, Z. Wang, J. E. Huang, J. Wicks, C. McCallum, N. Wang, Y. Wang, T. Chen, B. T. W. Lo, D. Sinton, J. C. Yu, Y. Wang and E. H. Sargent, *Nat. Catal.*, 2022, **5**, 564–570.

43 N. B. Watkins, Y. Wu, W. Nie, J. C. Peters and T. Agapie, *ACS Energy Lett.*, 2023, **8**, 189–195.

44 M. Sun, J. Cheng and M. Yamauchi, *Nat. Commun.*, 2024, **15**, 491.

45 M. Fan, J. E. Huang, R. K. Miao, Y. Mao, P. Ou, F. Li, X.-Y. Li, Y. Cao, Z. Zhang, J. Zhang, Y. Yan, A. Ozden, W. Ni, Y. Wang, Y. Zhao, Z. Chen, B. Khatir, C. P. O'Brien, Y. Xu, Y. C. Xiao, G. I. N. Waterhouse, K. Golovin, Z. Wang, E. H. Sargent and D. Sinton, *Nat. Catal.*, 2023, **6**, 763–772.

46 S. Garg, Q. Xu, A. B. Moss, M. Mirolo, W. Deng, I. Chorkendorff, J. Drnec and B. Seger, *Energy Environ. Sci.*, 2023, **16**, 1631–1643.

47 J. Fan, B. Pan, J. Wu, C. Shao, Z. Wen, Y. Yan, Y. Wang and Y. Li, *Angew. Chem., Int. Ed.*, 2024, **63**, e202317828.

48 H. G. Qin, Y. F. Du, Y. Y. Bai, F. Z. Li, X. Yue, H. Wang, J. Z. Peng and J. Gu, *Nat. Commun.*, 2023, **14**, 5640.

49 M. Zeng, W. Fang, Y. Cen, X. Zhang, Y. Hu and B. Y. Xia, *Angew. Chem., Int. Ed.*, 2024, **63**, e202404574.

50 D. Gao, R. M. Arán-Ais, H. S. Jeon and B. Roldan Cuenya, *Nat. Catal.*, 2019, **2**, 198–210.

51 C. Chen, Y. Li and P. Yang, *Joule*, 2021, **5**, 737–742.

52 J. A. Rabinowitz and M. W. Kanan, *Nat. Commun.*, 2020, **11**, 5231.

53 X. Zou and J. Gu, *Chin. J. Catal.*, 2023, **52**, 14–31.

54 N. Ziv, A. N. Mondal, T. Weissbach, S. Holdcroft and D. R. Dekel, *J. Membr. Sci.*, 2019, **586**, 140–150.

55 H. Xue, Z. H. Zhao, P. Q. Liao and X. M. Chen, *J. Am. Chem. Soc.*, 2023, **145**, 16978–16982.

56 N. Ling, J. Zhang, M. Wang, Z. Wang, Z. Mi, S. Bin Dolmanan, M. Zhang, B. Wang, W. Ru Leow, J. Zhang and Y. Lum, *Angew. Chem., Int. Ed.*, 2023, **62**, e202308782.

57 J. Li and N. Kornienko, *Chem Catal.*, 2022, **2**, 29–38.

58 B. Sun, Z. Li, D. Xiao, H. Liu, K. Song, Z. Wang, Y. Liu, Z. Zheng, P. Wang, Y. Dai, B. Huang, A. Thomas and H. Cheng, *Angew. Chem., Int. Ed.*, 2024, **63**, e202318874.

59 Y. Qiao, W. Lai, K. Huang, T. Yu, Q. Wang, L. Gao, Z. Yang, Z. Ma, T. Sun, M. Liu, C. Lian and H. Huang, *ACS Catal.*, 2022, **12**, 2357–2364.

60 S. Feng, X. Wang, D. Cheng, Y. Luo, M. Shen, J. Wang, W. Zhao, S. Fang, H. Zheng, L. Ji, X. Zhang, W. Xu, Y. Liang, P. Sautet and J. Zhu, *Angew. Chem., Int. Ed.*, 2024, **63**, e202317942.

61 X. Zi, Y. Zhou, L. Zhu, Q. Chen, Y. Tan, X. Wang, M. Sayed, E. Pensa, R. A. Geioughy, K. Liu, J. Fu, E. Cortes and M. Liu, *Angew. Chem., Int. Ed.*, 2023, **62**, e202309351.

62 H. Shen, H. Jin, H. Li, H. Wang, J. Duan, Y. Jiao and S. Z. Qiao, *Nat. Commun.*, 2023, **14**, 2843.

63 W. Nie, G. P. Heim, N. B. Watkins, T. Agapie and J. C. Peters, *Angew. Chem., Int. Ed.*, 2023, **62**, e202216102.

64 M. Ramdin, A. R. T. Morrison, M. de Groen, R. van Haperen, R. de Kler, E. Irtem, A. T. Laitinen, L. J. P. van den Broeke, T. Breugelmans, J. P. M. Trusler, W. D. Jong and T. J. H. Vlugt, *Ind. Eng. Chem. Res.*, 2019, **58**, 22718–22740.

65 H. Yano, F. Shirai, M. Nakayama and K. Ogura, *J. Electroanal. Chem.*, 2002, **533**, 113–118.

66 J. Shen, R. Kortlever, R. Kas, Y. Y. Birdja, O. Diaz-Morales, Y. Kwon, I. Ledezma-Yanez, K. J. P. Schouten, G. Mul and M. T. M. Koper, *Nat. Commun.*, 2015, **6**, 8177.

67 Y. Wu, K. Kamiya, T. Hashimoto, R. Sugimoto, T. Harada, K. Fujii and S. Nakanishi, *Electrochemistry*, 2020, **88**, 359–364.

68 H. Ooka, M. C. Figueiredo and M. T. M. Koper, *Langmuir*, 2017, **33**, 9307–9313.

69 D. M. Weekes, D. A. Salvatore, A. Reyes, A. Huang and C. P. Berlinguet, *Acc. Chem. Res.*, 2018, **51**, 910–918.

70 L. Yuan, S. Zeng, X. Zhang, X. Ji and S. Zhang, *Mater. Rep.: Energy*, 2023, **3**, 100177.

71 D. Xu, K. Li, B. Jia, W. Sun, W. Zhang, X. Liu and T. Ma, *Carbon Energy*, 2022, **5**, e230.

72 S. Zhu, T. Li, W.-B. Cai and M. Shao, *ACS Energy Lett.*, 2019, **4**, 682–689.

73 A. Vasileff, X. Zhi, C. Xu, L. Ge, Y. Jiao, Y. Zheng and S.-Z. Qiao, *ACS Catal.*, 2019, **9**, 9411–9417.

74 Y. Zheng, A. Vasileff, X. Zhou, Y. Jiao, M. Jaroniec and S. Z. Qiao, *J. Am. Chem. Soc.*, 2019, **141**, 7646–7659.

75 Y. Jiang, H. Li, C. Chen, Y. Zheng and S.-Z. Qiao, *ACS Catal.*, 2024, **14**, 8310–8316.

76 H. Li, H. Li, P. Wei, Y. Wang, Y. Zang, D. Gao, G. Wang and X. Bao, *Energy Environ. Sci.*, 2023, **16**, 1502–1510.

77 Y. Fu, Q. Xie, L. Wan, Q. Huang and J. Luo, *Mater. Today Energy*, 2022, **29**, 101105.

78 P. Moreno-Garcia, N. Kovacs, V. Grozovski, M. J. Galvez-Vazquez, S. Vesztergom and P. Broekmann, *Anal. Chem.*, 2020, **92**, 4301–4308.

79 M. H. Hicks, W. Nie, A. E. Boehme, H. A. Atwater, T. Agapie and J. C. Peters, *J. Am. Chem. Soc.*, 2024, **146**, 25282–25289.

80 M. C. O. Monteiro, A. Mirabal, L. Jacobse, K. Doblhoff-Dier, S. C. Barton and M. T. M. Koper, *JACS Au*, 2021, **1**, 1915–1924.

81 B. Pan, J. Fan, J. Zhang, Y. Luo, C. Shen, C. Wang, Y. Wang and Y. Li, *ACS Energy Lett.*, 2022, **7**, 4224–4231.

82 W. Zheng, *ACS Energy Lett.*, 2023, **8**, 1952–1958.

83 J. Li, G. Chen, Y. Zhu, Z. Liang, A. Pei, C.-L. Wu, H. Wang, H. R. Lee, K. Liu, S. Chu and Y. Cui, *Nat. Catal.*, 2018, **1**, 592–600.

84 X. Chen, J. Chen, N. M. Alghoraibi, D. A. Henckel, R. Zhang, U. O. Nwabara, K. E. Madsen, P. J. A. Kenis, S. C. Zimmerman and A. A. Gewirth, *Nat. Catal.*, 2020, **4**, 20–27.

85 F. Zhang and A. C. Co, *Angew. Chem., Int. Ed.*, 2020, **59**, 1674–1681.

86 S. Dieckhofer, D. Ohl, J. R. C. Junqueira, T. Quast, T. Turek and W. Schuhmann, *Chem. – Eur. J.*, 2021, **27**, 5906–5912.

87 T. Luo, K. Liu, J. Fu, S. Chen, H. Li, H. Pan and M. Liu, *Adv. Energy Sustainability Res.*, 2022, **4**, 2200148.

88 M. C. O. Monteiro, M. F. Philips, K. J. P. Schouten and M. T. M. Koper, *Nat. Commun.*, 2021, **12**, 4943.

89 Z. Xu, M. Sun, Z. Zhang, Y. Xie, H. Hou, X. Ji, T. Liu, B. Huang and Y. Wang, *ChemCatChem*, 2022, **14**, e202200052.

90 W. Ge, L. Dong, C. Wang, Y. Zhu, Z. Liu, H. Jiang and C. Li, *ACS Catal.*, 2024, **14**, 10529–10537.

91 A. Wang, W. Ge, W. Sun, X. Sheng, L. Dong, W. Zhang, H. Jiang and C. Li, *Angew. Chem., Int. Ed.*, 2024, **64**, e202412754.

92 Q. Zhang, X. Shao, J. Yi, Y. Liu and J. Zhang, *Chin. J. Chem. Eng.*, 2020, **28**, 2549–2554.

93 C. M. Gunathunge, V. J. Ovalle and M. M. Waegele, *Phys. Chem. Chem. Phys.*, 2017, **19**, 30166–30172.

94 M. C. O. Monteiro, F. Dattila, N. Lopez and M. T. M. Koper, *J. Am. Chem. Soc.*, 2022, **144**, 1589–1602.

95 Z.-M. Zhang, T. Wang, Y.-C. Cai, X.-Y. Li, J.-Y. Ye, Y. Zhou, N. Tian, Z.-Y. Zhou and S.-G. Sun, *Nat. Catal.*, 2024, **7**, 807–817.

96 J. J. Masana, B. Peng, Z. Shuai, M. Qiu and Y. Yu, *J. Mater. Chem. A*, 2022, **10**, 1086–1104.

97 T. Kim and G. T. R. Palmore, *Nat. Commun.*, 2020, **11**, 3622.

98 J. Resasco, Y. Lum, E. Clark, J. Z. Zeledon and A. T. Bell, *ChemElectroChem*, 2018, **5**, 1064–1072.

99 X. Zhou, J. Shan, L. Chen, B. Y. Xia, T. Ling, J. Duan, Y. Jiao, Y. Zheng and S. Z. Qiao, *J. Am. Chem. Soc.*, 2022, **144**, 2079–2084.

100 Q. Fan, G. Bao, X. Chen, Y. Meng, S. Zhang and X. Ma, *ACS Catal.*, 2022, **12**, 7517–7523.

101 L. P. Chi, Z. Z. Niu, Y. C. Zhang, X. L. Zhang, J. Liao, Z. Z. Wu, P. C. Yu, M. H. Fan, K. B. Tang and M. R. Gao, *Proc. Natl. Acad. Sci. U. S. A.*, 2023, **120**, e2312876120.

102 X. Li, P. Zhang, L. Zhang, G. Zhang, H. Gao, Z. Pang, J. Yu, C. Pei, T. Wang and J. Gong, *Chem. Sci.*, 2023, **14**, 5602–5607.

103 Z. Liu, T. Yan, H. Shi, H. Pan, Y. Cheng and P. Kang, *ACS Appl. Mater. Interfaces*, 2022, **14**, 7900–7908.

104 C. Zhu, G. Wu, A. Chen, G. Feng, X. Dong, G. Li, S. Li, Y. Song, W. Wei and W. Chen, *Energy Environ. Sci.*, 2024, **17**, 510–517.

105 S. Li, X. Dong, G. Wu, Y. Song, J. Mao, A. Chen, C. Zhu, G. Li, Y. Wei, X. Liu, J. Wang, W. Chen and W. Wei, *Nat. Commun.*, 2024, **15**, 6101.

106 T. Yan, H. Pan, Z. Liu and P. Kang, *Small*, 2023, **19**, 2207650.

107 Q. Wu, J. Liang, L. L. Han, Y. B. Huang and R. Cao, *Chem. Commun.*, 2023, **59**, 5102–5105.

108 R. Wang, L.-Z. Dong, J.-W. Shi, M. Zhang, S.-L. Li, Y.-Q. Lan and J. Liu, *ACS Catal.*, 2024, **14**, 741–750.

109 J. Feng, L. Wu, X. Song, L. Zhang, S. Jia, X. Ma, X. Tan, X. Kang, Q. Zhu, X. Sun and B. Han, *Nat. Commun.*, 2024, **15**, 4821.

110 X. Yu, Y. Xu, L. Li, M. Zhang, W. Qin, F. Che and M. Zhong, *Nat. Commun.*, 2024, **15**, 1711.

111 Y. Yang, J. Zhang, Z. Tan, J. Yang, S. Wang, M. Li and Z. Su, *Angew. Chem., Int. Ed.*, 2024, **63**, e202408873.

112 J. Zhang, C. Guo, S. Fang, X. Zhao, L. Li, H. Jiang, Z. Liu, Z. Fan, W. Xu, J. Xiao and M. Zhong, *Nat. Commun.*, 2023, **14**, 1298.

113 B. Han, Y. Wu, C. Chen, S. Liu, Q. Qian, Q. Zhu, R. Feng, L. Jing, X. Kang and X. Sun, *Angew. Chem., Int. Ed.*, 2024, **63**, e202410659.

114 M. Wang, B. Wang, J. Zhang, S. Xi, N. Ling, Z. Mi, Q. Yang, M. Zhang, W. R. Leow, J. Zhang and Y. Lum, *Nat. Commun.*, 2024, **15**, 1218.

115 Y. Chen, X. Y. Li, Z. Chen, A. Ozden, J. E. Huang, P. Ou, J. Dong, J. Zhang, C. Tian, B. H. Lee, X. Wang, S. Liu, Q. Qu, S. Wang, Y. Xu, R. K. Miao, Y. Zhao, Y. Liu, C. Qiu, J. Abed, H. Liu, H. Shin, D. Wang, Y. Li, D. Sinton and E. H. Sargent, *Nat. Nanotechnol.*, 2023, **19**, 311–318.

116 Z. Jiang, Z. Zhang, H. Li, Y. Tang, Y. Yuan, J. Zao, H. Zheng and Y. Liang, *Adv. Energy Mater.*, 2023, **13**, 2203603.

117 M. Fan, R. K. Miao, P. Ou, Y. Xu, Z. Y. Lin, T. J. Lee, S. F. Hung, K. Xie, J. E. Huang, W. Ni, J. Li, Y. Zhao, A. Ozden, C. P. O'Brien, Y. Chen, Y. C. Xiao, S. Liu, J. Wicks, X. Wang, J. Abed, E. Shirzadi, E. H. Sargent and D. Sinton, *Nat. Commun.*, 2023, **14**, 3314.

118 Q. Zhang, C. B. Musgrave, Y. Song, J. Su, L. Huang, L. Cheng, G. Li, Y. Liu, Y. Xin, Q. Hu, G. Ye, H. Shen, X. Wang, B. Z. Tang, W. A. Goddard and R. Ye, *Nat. Synth.*, 2024, **3**, 1231–1242.

119 M. D. Zhang, J. R. Huang, W. Shi, P. Q. Liao and X. M. Chen, *Angew. Chem., Int. Ed.*, 2023, **62**, e202308195.

120 Q. Wu, D. H. Si, J. Liang, Y. B. Huang and R. Cao, *Appl. Catal., B*, 2023, **333**, 122803.

121 C. P. Wan, H. Guo, D. H. Si, S. Y. Gao, R. Cao and Y. B. Huang, *JACS Au*, 2024, **4**, 2514–2522.

122 Y. Wang, C. Wang, Y. Wei, F. Wei, L. Kong, J. Feng, J. Q. Lu, X. Zhou and F. Yang, *Chem. – Eur. J.*, 2022, **28**, e202201832.

123 S. Li, G. Wu, J. Mao, A. Chen, X. Liu, J. Zeng, Y. Wei, J. Wang, H. Zhu, J. Xia, X. Wang, G. Li, Y. Song, X. Dong, W. Wei and W. Chen, *Angew. Chem., Int. Ed.*, 2024, **63**, e202407612.

124 J.-N. Zhang, N. K. Niazi, J. Qiao, L. Li, I. M. U. Hasan, R. He, L. Peng, N. Xu and F. Farwa, *Nano Res. Energy*, 2022, **1**, e9120015.

125 Y. Jiang, J. Shan, P. Wang, L. Huang, Y. Zheng and S.-Z. Qiao, *ACS Catal.*, 2023, **13**, 3101–3108.

126 G. Neri, I. M. Aldous, J. J. Walsh, L. J. Hardwick and A. J. Cowan, *Chem. Sci.*, 2016, **7**, 1521–1526.

127 X. Sheng, W. Ge, H. Jiang and C. Li, *Adv. Mater.*, 2022, **34**, 2201295.

128 M. Wang, Z. Wang, Z. Huang, M. Fang, Y. Zhu and L. Jiang, *ACS Nano*, 2024, **18**, 15303–15311.

129 Z. Wang, Y. Li, X. Zhao, S. Chen, Q. Nian, X. Luo, J. Fan, D. Ruan, B. Q. Xiong and X. Ren, *J. Am. Chem. Soc.*, 2023, **145**, 6339–6348.

130 M. Zhang, J. Wang, X. Rong, X.-L. Lu and T.-B. Lu, *Nano Res.*, 2024, **17**, 2381–2387.

131 K. Xu, J. Li, F. Liu, X. Chen, T. Zhao and F. Cheng, *Angew. Chem., Int. Ed.*, 2023, **62**, e202311968.

132 X. Zhao, H. Xie, B. Deng, L. Wang, Y. Li and F. Dong, *Chem. Commun.*, 2024, **60**, 542–545.

133 E. Vichou, A. Perazio, Y. Adjez, M. Gomez-Mingot, M. W. Schreiber, C. M. Sánchez-Sánchez and M. Fontecave, *Chem. Mater.*, 2023, **35**, 7060–7068.

134 H. Jin, J. Xu, H. Liu, H. Shen, H. Yu, M. Jaroniec, Y. Zheng and S. Z. Qiao, *Sci. Adv.*, 2023, **9**, eadi7755.

135 C. Peng, H. Shen, M. Zheng, M. Jaroniec, Y. Zheng and S.-Z. Qiao, *ACS Catal.*, 2024, **15**, 468–476.

136 X. Fan, C. Liu, X. He, Z. Li, L. Yue, W. Zhao, J. Li, Y. Wang, T. Li, Y. Luo, D. Zheng, S. Sun, Q. Liu, L. Li, W. Chu, F. Gong, B. Tang, Y. Yao and X. Sun, *Adv. Mater.*, 2024, **36**, 2401221.

137 Z. Zhang, D. Li, Y. Tu, J. Deng, H. Bi, Y. Yao, Y. Wang, T. Li, Y. Luo, S. Sun, D. Zheng, S. A. C. Carabineiro, Z. Chen, J. Zhu and X. Sun, *SusMat*, 2024, **4**, e193.